Aeroelastic and Aerothermoelastic Behavior in Hypersonic Flow

Jack J. McNamara,* Peretz P. Friedmann,† Kenneth G. Powell,‡ and Biju J. Thuruthimattam§
University of Michigan, Ann Arbor, Michigan 48109
and
Robert E. Bartels¶
NASA Langley Research Center, Hampton, Virginia 23681

The testing of aeroelastically and aerothermoelastically scaled wind-tunnel models in hypersonic flow is not feasible; thus, computational aeroelasticity and aerothermoelasticity are essential to the development of hypersonic vehicles. Several fundamental issues in this area are examined by performing a systematic computational study of the hypersonic aeroelastic and aerothermoelastic behavior of a three-dimensional configuration. Specifically, the flutter boundary of a low-aspect-ratio wing, representative of a fin or control surface on a hypersonic vehicle, is studied over a range of altitudes using third-order piston theory and Euler and Navier–Stokes aerodynamics. The sensitivity of the computational-fluid-dynamics-based aeroelastic analysis to grid resolution and parameters governing temporal accuracy are considered. In general, good agreement at moderate-to-high altitudes was observed for the three aerodynamic models. However, the wing flutters at unrealistic Mach numbers in the absence of aerodynamic heating. Therefore, because aerodynamic heating is an inherent feature of hypersonic flight and the aeroelastic behavior of a vehicle is sensitive to structural variations caused by heating, an aerothermoelastic methodology is developed that incorporates the heat transfer between the fluid and structure based on computational-fluid-dynamics-generated aerodynamic heating. The aerothermoelastic solution procedure is then applied to the low-aspect-ratio wing operating on a representative hypersonic trajectory. In the latter study, the sensitivity of the flutter margin to perturbations in trajectory angle of attack and Mach number is considered. Significant reductions in the flutter boundary of the heated wing are observed. The wing is also found to be susceptible to thermal buckling.

Nomenclature

a_∞	=	speed of sound
$C_L, C_M,$	=	coefficients of lift and moment about the elastic
C_D		axis and drag
C_p	=	coefficient of pressure
CFL_τ	=	Courant–Friedrichs–Lewy three-dimensional input parameter regulating pseudo-time-step size
C_w	=	Chapman–Rubesin coefficient
c	=	reference chord length of the double-wedge airfoil
c_{pw}	=	specific heat of the wall
h_{ht}	=	heat-transfer coefficient
k_ω	=	reduced frequency
M	=	freestream Mach number
$\mathbf{M}, \mathbf{K}$	=	generalized mass and stiffness matrices of the structure
M_f	=	flutter Mach number
$\mathbf{n}$	=	normal vector
n_m	=	number of modes
p	=	pressure
p_∞	=	freestream pressure
$\mathbf{Q}$	=	generalized force vector for the structure
Q_i	=	generalized force corresponding to mode i
$\dot{q}_{\mathrm{aero}}, \dot{q}_{\mathrm{rad}},$	=	heat-transfer rate due to aerodynamic heating,
$\dot{q}_{\mathrm{cond}}, \dot{q}_{\mathrm{strd}}$		radiation, conduction, and stored energy
q_i	=	modal amplitude of mode i
q_{vf}	=	virtual-flutter dynamic pressure
q_∞	=	dynamic pressure
Re	=	Reynolds number
S	=	surface area of the structure
T	=	temperature
T_{AW}	=	adiabatic-wall temperature
T_E	=	kinetic energy of the structure
T_R	=	radiation equilibrium wall temperature
T_{ref}	=	reference temperature
T_W	=	wall temperature
T_0	=	stagnation temperature
T_∞	=	freestream temperature
t	=	time
U_E	=	potential energy of the structure
V	=	freestream velocity
v_n	=	normal velocity of airfoil surfaces
w	=	displacement of the surface of the structure
x, y, z	=	spatial coordinates
y^+	=	law-of-the-wall coordinate
$Z(x, y, t)$	=	position of structural surface
α_s	=	angle of attack
γ	=	ratio of specific heat
Δ_w	=	skin thickness
Δt	=	time step
ϵ	=	emissivity
ζ	=	damping ratio
κ	=	thermal conductivity
ρ	=	air density
ρ_W	=	wall density
σ	=	Stefan–Boltzmann constant
$\boldsymbol{\Phi}$	=	modal matrix
ϕ_i	=	mode shape for mode i
ω_i	=	frequency of mode i
$\dot{(\,)}, \ddot{(\,)}$	=	first and second derivatives with respect to time

*Postdoctoral Scholar, Department of Aerospace Engineering; currently Assistant Professor, Aerospace Engineering Department, Ohio State University, Columbus, OH. Member AIAA.

†François-Xavier Bagnoud Professor, Department of Aerospace Engineering. Fellow AIAA.

‡Arthur F. Thurnau Professor, Department of Aerospace Engineering. Associate Fellow AIAA.

§Postdoctoral Scholar, Department of Aerospace Engineering; currently Associate, Portfolio Management Group, BlackRock, Inc., New York, NY.

¶Senior Research Engineer, Aeroelasticity Branch.

I. Introduction

T HE first vehicle to fly at hypersonic speed was a WAC Corporal rocket launched from a U.S.-captured German V-2 rocket in February 1949 [1]. Currently, despite sizeable investments over the years in vehicles aimed at this flight regime, the ability of sustained hypersonic flight is still an unfulfilled goal. The idea of a single-stage-to-orbit reusable launch vehicle capable of using conventional runways, called the National Aerospace Plane (NASP), was examined in the mid-1980s. However, the program was canceled due to design requirements that exceeded the state of the art [1,2]. A more recent reusable launch vehicle project, the VentureStar program, failed during structural tests, again for lack of availability of appropriate technology. Despite these unsuccessful programs, the continued need for a low-cost single-stage-to-orbit or two-stage-to-orbit reusable launch vehicle, as well as the desire of the U.S. Air Force for unmanned hypersonic vehicles, has reinvigorated hypersonic flight research. Recent advances in supersonic combustion ramjet (scramjet) engines, as evident in the NASA Hyper-X experimental vehicle [3] and University of Queensland HyShot [4] efforts, have demonstrated the feasibility of this class of vehicles. In the FALCON [Force Application and Launch from CONUS (the continental United States)] program, the Defense Advanced Research Projects Agency (DARPA) and the U.S. Air Force intend to use scramjet technologies to develop, by 2025, an autonomous reusable hypersonic cruise vehicle that can strike targets at distances up to 9000 n mile within 2 h [5].

The conditions encountered in hypersonic flows, combined with the need to design hypersonic vehicles, have motivated research in the areas of hypersonic aeroelasticity and aerothermoelasticity. As indicated by Fig. 1, hypersonic vehicle configurations will consist of
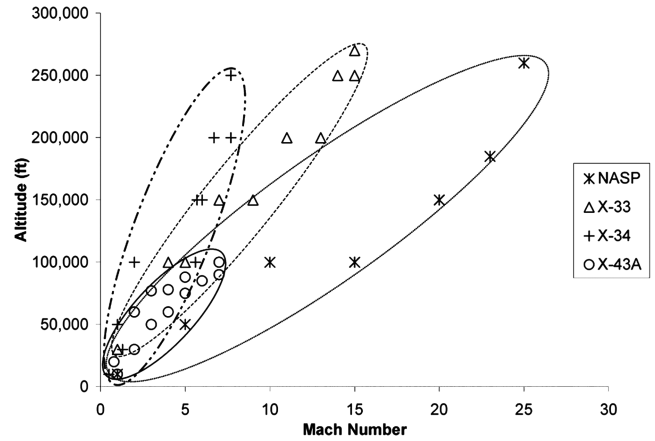

Fig. 2 Operating envelopes for several modern hypersonic vehicles.

long, slender, lifting-body designs. In general, the body and aerodynamic control surfaces will be flexible due to minimum-weight restrictions. Furthermore, as shown in Fig. 2, these vehicles operate [6–9] over a Mach number range of 0 to 15 and must fly within the atmosphere for sustained periods of time to meet the needs of an airbreathing propulsion system [10]. The combined extreme aerodynamic heating and loading acting on the airframe produce complex interactions between the flow, dynamics, structure, control, and propulsion systems. These interactions have received only limited attention in the past. Moreover, the impracticality of testing aeroelastically and aerothermoelastically scaled models in wind
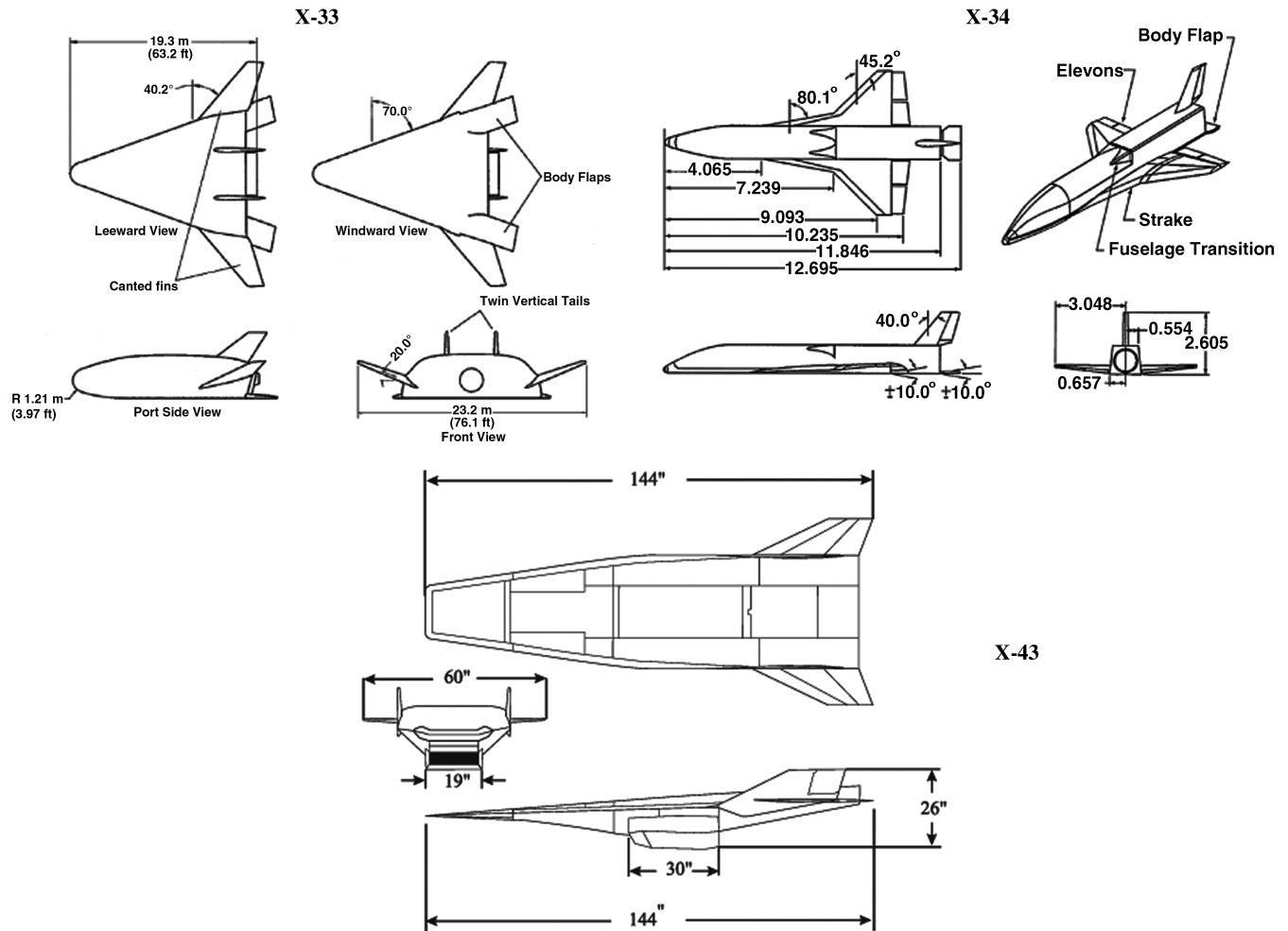

Fig. 1 Schematic description of several hypersonic vehicles.

tunnels [11], a common practice in the subsonic and supersonic flow regimes, implies that aeroelastic simulations are critical for the development of vehicles intended for this flight regime.

Hypersonic aeroelasticity and aerothermoelasticity was an active area of research in the late 1950s and during the 1960s, as evident from [12–16]. This research was instrumental in providing the basis for the aerothermoelastic design of the space shuttle. This early research has been followed by periods of inactivity as well as spurts of activity that have produced a body of knowledge that can be separated into several categories or groups. The first category consists of studies focusing on panel flutter, which is a localized aeroelastic problem representing a small portion of the skin on the surface of the hypersonic vehicle [17–22]. The second group of studies in this area was motivated by a previous hypersonic vehicle: namely, the NASP [6,23–28]. In these studies, the hypersonic aeroelastic analysis was carried out using a finite element structural model of the vehicle in conjunction with piston theory aerodynamics [6]. Some of these studies [26–28] examined simplified aerothermoelastic behavior of NASP-like configurations using approximate steady-state surface temperatures to account for aerodynamic heating effects. These studies found that aerodynamic heating alters the aeroelastic stability of the vehicle through a combination of the degradation of material properties and introduction of thermal stresses [26–28].

The third group is restricted to more recent papers that deal with the newer hypersonic configurations such as the X-33 or the X-34. Reference [29] considered the X-34 launch vehicle in free flight at $M = 8.0$. In [7], a CFD-based aeroelastic analysis was carried out on the X-43 vehicle using an autoregressive moving-average (ARMA) system-identification-based order reduction of the aerodynamic degrees of freedom. Both the structure and the fluid were discretized using the finite element approach. It was shown that piston theory and ARMA reduced-order Euler calculations predicted somewhat similar flutter behavior. In [30], the aeroelastic stability of a generic hypersonic vehicle resembling the X-33 was considered using first-order piston theory. In a sequel to this study [31], the piston theory results for the aeroelastic behavior were also compared with aeroelastic stability boundaries obtained from computational aeroelasticity, and it was shown that the primitive aerodynamic model used in [30] was inadequate for hypersonic aeroelastic analysis.

The overall objective of this paper is to examine the fundamental aspects of hypersonic aeroelasticity and aerothermoelasticity using computational tools. This is accomplished by considering a relatively simple three-dimensional low-aspect-ratio wing, shown in Fig. 3, which is representative of a fin or control surface on the hypersonic vehicles depicted in Fig. 1. Such a configuration allows one to focus on basic modeling issues of hypersonic aeroelasticity and aerothermoelasticity without the additional effort required to generate results for a more complex structure. The specific objectives of the paper are as follows:

1) Examine the mesh requirements for reliable CFD solutions to the unsteady Euler and Navier–Stokes equations in the hypersonic flow regime.

2) Examine the sensitivity of the aeroelastic behavior of a low-aspect-ratio wing, generated using CFD solutions to the unsteady
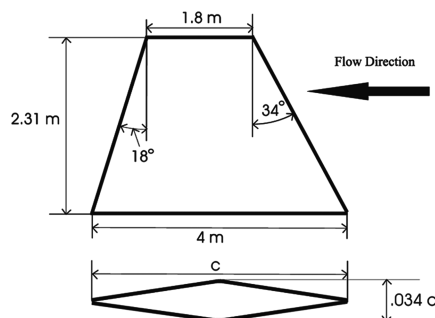
Euler and Navier–Stokes equations, to parameters governing temporal accuracy.

3) Obtain the stability boundaries for a low-aspect-ratio wing using unsteady Euler and Navier–Stokes aerodynamics and compare them with those obtained using third-order piston theory.

4) Develop a refined aerothermoelastic model that incorporates the effect of heat transfer between the structure and the fluid due to intense aerodynamic heating, and obtain the stability boundaries of a low-aspect-ratio wing for a representative hypersonic vehicle trajectory.

Achieving these objectives significantly enhances our understanding of hypersonic aeroelasticity and aerothermoelasticity.

II. Method of Solution

The computational aeroelastic solutions in the present study are obtained using the NASA Langley code CFL3D [32]. Specifically, the CFL3D code is used to generate both steady and unsteady air loads, and it also produces the aeroelastic transients and response solutions. The fluid–structure coupling in the code is accomplished using the free-vibration modes of the vehicle. A detailed description of the solution process is provided next.

A. Euler/Navier–Stokes Solver in CFL3D

The CFL3D code employs an implicit finite volume algorithm based on upwind-biased spatial differencing to solve the time-dependent Euler and Reynolds-averaged Navier–Stokes equations. Multigrid and mesh sequencing are available for convergence acceleration. The algorithm, which is based on a cell-centered scheme, uses upwind-differencing based on either flux-vector splitting or flux-difference splitting and can sharply capture shock waves. For applications using the thin-layer Navier–Stokes equations, different turbulence models are available. For time-accurate problems using a deforming mesh, an additional term accounting for the change in cell volume is included in the time discretization of the governing equations [33]. Because CFL3D is an implicit code using approximate factorization, linearization and factorization errors are introduced at every time step. Hence, intermediate calculations (referred to as subiterations) are used to reduce these errors. Increasing these subiterations improves the accuracy of the simulation, albeit at increased computational cost.

B. Aeroelastic Option in CFL3D

The aeroelastic approach underlying the CFL3D code is similar to that described in [34,35]. The equations are derived by assuming that the general motion $w(x, y, z, t)$ of the structure is described by a finite modal series given by Eq. (1). The functions $\phi_i(x, y, z)$ represent the free-vibration modes of the vehicle, which are calculated using a finite element approach:

$$w(x, y, z, t) = \sum_{i=1}^{n_m} q_i(t)\phi_i(x, y, z) \qquad (1)$$

The aeroelastic equations of motion are obtained from Lagrange's equations:

$$\frac{\mathrm{d}}{\mathrm{d}t}\left(\frac{\partial T_E}{\partial \dot{q}_i}\right) - \frac{\partial T_E}{\partial q_i} + \frac{\partial U_E}{\partial q_i} = Q_i, \qquad i = 1, 2, \ldots, n_m \qquad (2)$$

which yield

$$\mathbf{M}\,\ddot{\mathbf{q}} + \mathbf{K}\mathbf{q} = \mathbf{Q}(\mathbf{q}, \dot{\mathbf{q}}, \ddot{\mathbf{q}}), \qquad \mathbf{q}^T = [q_1 q_2 \cdots q_{n_m}] \qquad (3)$$

where the elements of the generalized force vector are given by

$$Q_i = \frac{\rho V^2}{2} c^2 \int_S \phi_i \frac{\Delta p(\mathbf{q}, \dot{\mathbf{q}}, \ddot{\mathbf{q}})\,\mathrm{d}S}{\rho V^2/2c^2} \qquad (4)$$

The aeroelastic equations are written in terms of a linear state-space equation (using a state vector of the form

Fig. 3 Planform and cross-sectional views of the low-aspect-ratio wing.

$[\cdots \dot{q}_{i-1} \quad q_i \quad \dot{q}_i \quad q_{i+1} \cdots]^T$) such that a modified state-transition-matrix integrator can be used to march the coupled fluid–structural system forward in time. At the beginning of each time step, the incremental structural deflections are calculated using the modal velocities and generalized aerodynamic forces. Using a deforming mesh, the mesh points are moved so that the inner mesh boundaries conform to the new deformed shape of the structure and the far-field boundaries are held stationary. The fluid equations, including the geometric-conservation-law terms, compute the flowfield throughout the updated mesh. The generalized aerodynamic forces acting on the structure through the next time step are then computed. Thus, tight coupling of the flow and the structure is implemented through the generalized aerodynamic forces. Finally, a time history of the modal displacements, modal velocities, and generalized forces is obtained.

The aeroelastic capabilities of CFL3D, based on this modal response approach for obtaining the flutter boundary, have been partially validated for the transonic regime for the first AGARD standard aeroelastic configuration for dynamic response, wing 445.6. The results of flutter calculations using Euler aerodynamics are given in [36] and those using Navier–Stokes aerodynamics are given in [37]. For more recent validation using the AGARD 445.6 wing flutter-onset envelope, the current version of CFL3D (version 6.0) was used in [38].

C. Computational Methods for Fluid–Structure Coupling

Prediction of the dynamic response of a flexible structure in a fluid requires the simultaneous solutions of the equations of motion of the structure and the fluid. To impose the kinematic boundary conditions on the fluid mesh at the new time step, the location and velocity of the fluid–structure boundary must first be known. This requires the solution of the entire system of equations for the structure, a task that cannot be carried out until the current surface pressure is known, which depends on the solution of the fluid domain and thus also on the unknown boundary conditions during the current time step. In addition, the discretized model of the structure uses a Lagrangian approach by following a point located on the structure over time, whereas the discretized model of the fluid uses an Eulerian approach by computing the flow quantities at a specific location in space over time. Therefore, accurate coupling of the two systems is a fairly complicated endeavor. A straightforward approach to the solution of the coupled fluid–structure system requires changing the fluid grid at each time step, which is computationally very expensive. Therefore, several different approaches have emerged as alternatives to partial regridding in transient aeroelastic computations, among them being dynamic meshes [39], the space–time formulation [40–42], the arbitrary/mixed Eulerian–Lagrangian formulation [43,44], the multiple-field formulation [45,46], the transpiration method [7,47], the exponential-decay/transfinite-interpolation (TFI) method [48,49], the modified spring analogy [33], and the finite macroelement method [49,50]. Note that the exponential-decay/TFI, modified spring analogy, and finite macroelement methods are all available in the CFL3D code for fluid–structural coupling [33,49,50].

This study implements the exponential-decay/TFI approach [48,49], which is an algebraic mesh deformation method in which surface movement is transmitted into the mesh interior using an exponential-decay function. The motion of selected slave points, chosen across a grid at constant index intervals, is tied to the motion of the nearest surface (or master) point. The exponential-decay function uses distance between the slave and nearest surface point so that motion of the surface is transmitted nearly undiminished to nearby slave points. Intervening mesh points on block faces are updated using TFI, a scheme [51] that efficiently maps grid displacements from one block face to another using polynomial functions. Once the intermediate mesh between slave points is updated on block faces, block interiors are updated using a volume TFI step. When smoothing of the deformed grid is necessary, several iterations of a modified spring analogy are employed. This scheme is a modification of the spring analogy [39] by using axial spring

stiffness. Spring stiffness in the mesh interior is controlled by the spacing of the appropriate boundary grid points. Note that the axial stiffness approach results in smoothing of the mesh and also allows adaptation based on the flow solution. Furthermore, the problem of grid collapse around convex surfaces is handled by selectively increasing/decreasing stiffness based on surface curvature.

Note that during the mesh deformation process, the code ensures that the generated control points at block boundaries are coincident and also checks block boundaries for separation during the mesh deformation at each time step [49].

D. General Overview of the Solution Process

The solution of the computational aeroelasticity problem considered in the present study is shown in Fig. 4. First, the vehicle geometry is created using CAD software, and from this geometry, a mesh generator is used to create a structured mesh for the flow domain around the body. In parallel, an unstructured mesh is generated that represents the surface of the finite element model of the vehicle. This structural model is further refined with internal stiffeners and mass elements to represent an actual structure and is used to obtain the free-vibration modes using MSC.Nastran. Subsequently, the fluid mesh is used to compute the flow around the rigid vehicle using the steady CFD solver in CFL3D. To generate the structural input for the aeroelastic solver in CFL3D, the modal deformation at each surface grid point in the fluid mesh is obtained by using cubic interpolation (in MATLAB) from the finite element structural model for each structural mode. Using the flow solution as an initial condition and the interpolated modal data as additional input, an aeroelastic equilibrium state is obtained for the flexible vehicle. For a geometry with vertical symmetry at a 0-deg angle of attack, the equilibrium state is the same as the undeflected state. Next, the structure is perturbed in one or more of its modes by an initial modal velocity condition, and the transient response of the structure is obtained. To determine the flutter conditions at a given altitude, aeroelastic transients are computed at several Mach numbers and the corresponding dynamic pressures. The frequency and damping characteristics of the transient response for a given flight condition and vehicle configuration are determined using the ARMA method of time-domain damping and frequency identification [52–56]. This approach applied at the same altitude and vehicle configuration for a range of Mach numbers results in a series of damping values for the
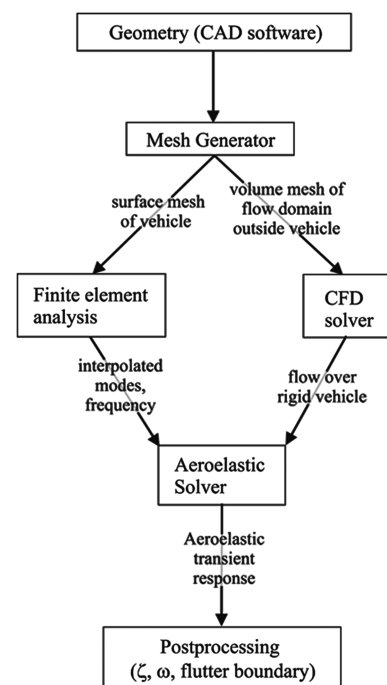

Fig. 4 A flow diagram of the computational aeroelastic solution procedure.

Table 1 Comparison of the Lockheed F-104 Starfighter wing with the low-aspect-ratio-wing model

Parameter	F-104	Model
Wing mass, kg	350.28	350.05
First bending frequency, Hz	13.40	13.41
First torsional frequency, Hz	37.60	37.51

system. The flutter Mach number can be estimated from this series by interpolating the damping data points to identify the value of the Mach number at which the damping is zero.

E. Piston Theory

Piston theory is a simple inviscid unsteady aerodynamic theory that has been used extensively in supersonic and hypersonic aeroelasticity. It provides a point-function relationship between the local pressure on the surface of the vehicle and the component of fluid velocity at the moving surface normal to the freestream direction [57,58]. The derivation uses the isentropic simple wave expression for the pressure on the surface of a moving piston:

$$\frac{p(x,t)}{p_\infty} = \left(1 + \frac{\gamma-1}{2}\frac{v_n}{a_\infty}\right)^{\frac{2\gamma}{(\gamma-1)}} \quad (5)$$

where

$$v_n = \frac{\partial Z(x,y,t)}{\partial t} + V\frac{\partial Z(x,y,t)}{\partial x} \quad (6)$$

The expression for piston theory is based on a binomial expansion of Eq. (5), in which the order of the expansion is determined by the ratio of v_n/a_∞. Reference [58] suggested a third-order expansion, because it produced the smallest error of the various orders of expansion used when compared with the limiting values of pressure: namely, the simple wave and shock expansion solutions. The third-order expansion of Eq. (5) yields third-order piston theory:

$$C_p(x,t) = \frac{2}{M_\infty^2}\left\{\frac{v_n}{a_\infty} + \frac{(\gamma+1)}{4}\left(\frac{v_n}{a_\infty}\right)^2 + \frac{(\gamma+1)}{12}\left(\frac{v_n}{a_\infty}\right)^3\right\} \quad (7)$$

F. Structural Model of the Low-Aspect-Ratio Wing

The structural model for the low-aspect-ratio wing is based on the Lockheed F-104 Starfighter wing. It was developed with finite elements in MSC.Nastran by matching its total mass and first bending and torsional frequencies to the corresponding F-104 wing values. A comparison of the final model values with the F-104 wing is provided in Table 1, and the first 5 natural frequencies and modes are shown in Fig. 5. Note that the wing structure was assumed to be made from 2024-T3 aluminum alloy.

The finite element structural model, shown in Fig. 6, has 1327 total degrees of freedom, with 20 CTRIA3 (6 surface elements) and 1700
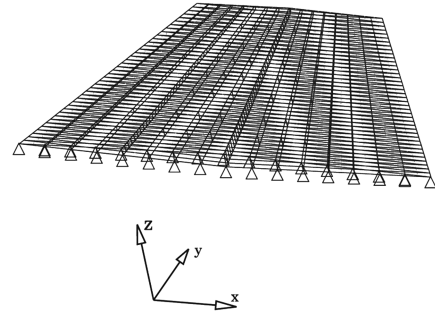

Fig. 6 Finite element model of the low-aspect-ratio wing, showing boundary conditions.

CQUAD4 (1318 surface elements) bilinear plate flexural elements. Stiffeners were placed throughout the structure using CTRIA3 and CQUAD4 elements to prevent breathing modes and to tune the model frequencies to those listed in Table 1. Finally, it is important to mention that the rigid-body modes were suppressed by cantilevering the wing at the root and are not considered in this study.

G. Refined Aerothermoelastic Model

A practical aeroelastic model for the hypersonic regime must include aerodynamic heating effects. Aerodynamic heating significantly alters the flow properties [59], degrades the material properties, and introduces thermal stresses [13,60–63]. Aerodynamic heating of the flow surrounding the vehicle leads to significantly different thermodynamic and transport properties, high heat-transfer rates, variable γ, possible ionization, and nonadiabatic effects from radiation [59,60]. Thermal stresses can arise from rapidly changing conditions of heat input in which time lags are involved or from equilibrium conditions of nonuniform temperature distribution [13,61–63]. Commonly, the heated structure has lower stiffness due to material degradation and thermal stresses, which manifest themselves as a reduction in frequencies [13,61,64–66].

An exact treatment of aerothermoelasticity requires the coupling of the unsteady heat-transfer problem with the aeroelastic problem based on a Navier–Stokes solution of the unsteady airloads, which results in time-dependent temperature distributions. This implies time-dependent free-vibration characteristics of a structure at a given Mach number as it is heated.

The heat transfer between the fluid and the structure, schematically depicted in Fig. 7, is determined from an energy balance of the heat fluxes at the wall of the structure [10,62,63]:

$$\dot{q}_{\text{aero}} = \dot{q}_{\text{rad}} + \dot{q}_{\text{cond}} + \dot{q}_{\text{strd}} \quad (8)$$

where

$$\dot{q}_{\text{aero}} = h_{\text{ht}}(T_{\text{AW}} - T_W) \quad (9)$$

a) Mode 1, first bending, 13.41 Hz   b) Mode 2, first torsion, 37.51 Hz   c) Mode 3, second bending, 49.18 Hz

d) Mode 4, second torsion, 77.14 Hz   e) Mode 5, third torsion, 79.48 Hz
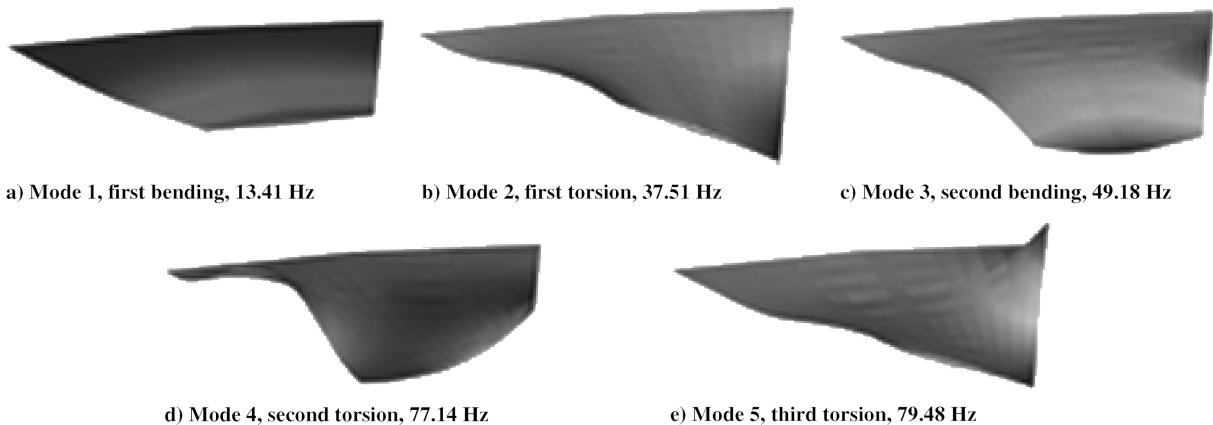
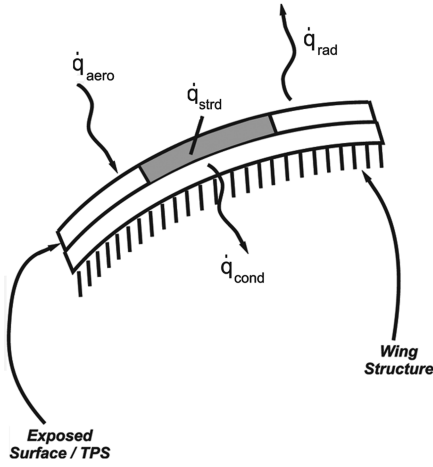**Fig. 5 First 5 free-vibration modes of the low-aspect-ratio wing.**

Fig. 7   Heat transfer at the wall of a hypersonic vehicle.

$$\dot{q}_{\text{rad}} = \sigma \epsilon T_W^4 \tag{10}$$

$$\dot{q}_{\text{cond}} = \left(\kappa \frac{\partial T}{\partial \mathbf{n}} \right)_W \tag{11}$$

$$\dot{q}_{\text{strd}} = \rho_W c_{pw} \Delta_w \frac{\mathrm{d}T_W}{\mathrm{d}t} \tag{12}$$

The heat transfer represents a balance at the wall between the convective heating by the fluid ($\dot{q}_{\text{aero}}$) and heat loss due to conduction into the structure ($\dot{q}_{\text{cond}}$), radiation out to space ($\dot{q}_{\text{rad}}$), and energy stored in the wall ($\dot{q}_{\text{strd}}$). The heat-transfer problem is driven by Eq. (9) or, more specifically, the adiabatic-wall temperature T_{AW}, which is a function of the surface geometry and freestream conditions. Note that at steady state,

$$\dot{q}_{\text{aero}} = \dot{q}_{\text{rad}} \tag{13}$$

Therefore, using Eqs. (9) and (10),

$$\sigma \epsilon T_R^4 - h_{\text{ht}} T_R - h_{\text{ht}} T_{\text{AW}} = 0 \tag{14}$$

where, given h_{ht}, T_{AW}, σ, and ϵ, the radiation equilibrium temperature at the wall, T_R, can be determined by solving a fourth-order algebraic equation.

The solution procedure for the refined aerothermoelastic system is depicted in Fig. 8. Comparing Figs. 4 and 8a illustrates the modification introduced by the aerothermoelastic solution, in which aerodynamic heating information [T_{AW} and h_{ht} from Eq. (9)], obtained from rigid-body CFD computations, is introduced into the finite element analysis of the system. Specifically, T_{AW} is calculated by specifying an adiabatic wall as a boundary condition for the CFD solution to the Navier–Stokes equations, and h_{ht} is calculated from a separate Navier–Stokes solution in which the wall-temperature boundary condition is set to the freestream temperature. Setting a freestream, or cold, wall boundary condition to calculate h_{ht} provides a conservative estimate of the aerodynamic heating [67]. The transient temperature distribution in the structure is determined from a heat-transfer analysis using finite element analysis, and the free-vibration frequency and mode shapes of the transiently heated structure are then calculated at each desired point in time. This process is depicted in Fig. 8b. Note that both material-property degradations and thermal-stress effects are included in the computation of the heated free-vibration frequencies and mode shapes.

It is important to mention that this is not an exact treatment of the aerothermoelastic system, because the temperature distribution is not computed at each time step of the aeroelastic calculation procedure. It is, however, a reasonable approximation, because the heat loads vary
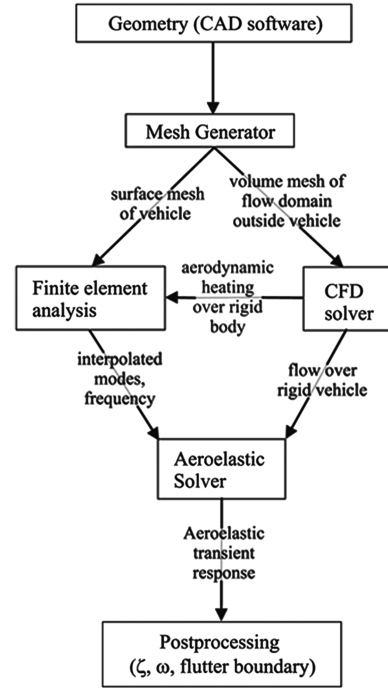
a) Aerothermoelastic solution procedure
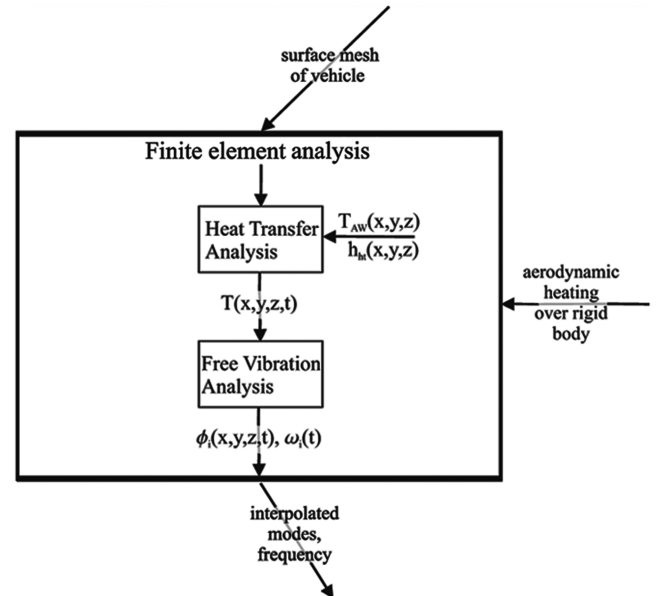
b) Finite element analysis

Fig. 8   A flow diagram for the computational aerothermoelastic solution procedure. The aerodynamic heating information is passed from the CFD solver to the finite element analysis module; to compute the heat transfer between the fluid and structure, and heated free-vibration characteristics.

slowly with time, compared with the generalized forces and motion of the system. Furthermore, it is computationally prohibitive to generate an aeroelastic simulation continuously for the timescales involved to heat the structure.

III.   Results and Discussion

As stated in the Introduction, the goal of this paper is to study several fundamental aspects of hypersonic aeroelasticity and aerothermoelasticity. As a first step, the aeroelastic behavior of a low-aspect-ratio wing, shown in Fig. 3, is studied using piston theory aerodynamics. Using this analysis as a reference point, a CFD-based aeroelastic analysis of the wing is carried using the CFL3D code.

During this analysis, issues pertaining to grid convergence and temporal accuracy in hypersonic flow are investigated. The flutter boundary of the wing is then computed over a range of operating altitudes using third-order piston theory and Euler and Navier–Stokes aerodynamics. Finally, aerodynamic heating is incorporated into the hypersonic aeroelastic analysis of the low-aspect-ratio wing using the refined aerothermoelastic model.

A. Preliminary Aeroelastic Analysis of the Low-Aspect-Ratio Wing

To gain insight into its flutter characteristics in hypersonic flow, a preliminary aeroelastic analysis of the low-aspect-ratio wing was carried out using piston theory aerodynamics. First, the sensitivity of the wing's aeroelastic behavior to the number of structural modes used in the system was examined. Using third-order piston theory in conjunction with 2, 5, and 8 structural modes, the flutter Mach number was predicted to be $M_f = 15.6$, 13.4, and 13.3, respectively (40,000 ft). It is evident that increasing the number of modes from 2 to 5 results in a significant reduction in the flutter Mach number of the wing, whereas increasing the modes from 5 to 8 has a minimal effect. Thus, the aeroelastic analysis conducted in the rest of this paper was carried out using 5 structural modes.

The damping and frequency characteristics of the low-aspect-ratio wing at 40,000 ft are shown in Fig. 9, in which first-order ($M_f = 23.8$) and third-order ($M_f = 13.4$) piston theory was used to compute the unsteady generalized aerodynamic forces. In both the first-order and third-order cases, there is a coalescence in frequency with increasing Mach number for the first bending (mode 1) and first torsion (mode 2) modes. Simultaneously, the damping of the first mode approaches zero, whereas the damping of mode 2 increases. The damping and frequencies of modes 3–5 are relatively constant with increasing Mach number.

It is important to note that despite similar trends in damping and frequency, first-order piston theory predicts a flutter Mach number that is 80% higher than the third-order piston theory result. Also, it is clear from these results that the wing flutters at relatively high Mach numbers at low altitudes. Finally, it is interesting to calculate the reduced frequencies of the system at the flutter Mach number predicted using third-order piston theory. Using the frequency of the flutter mode, this corresponds to $k_\omega = 0.14$, whereas for mode 5, $k_\omega = 0.51$. Therefore, it is evident that the reduced frequency of the flutter mode in hypersonic flow is relatively small.

B. Grid Convergence Studies for Computational Aeroelasticity in Hypersonic Flow

In CFD computations, fluid mesh quality is critical for the accurate prediction of aerodynamic loads. The development of an appropriate
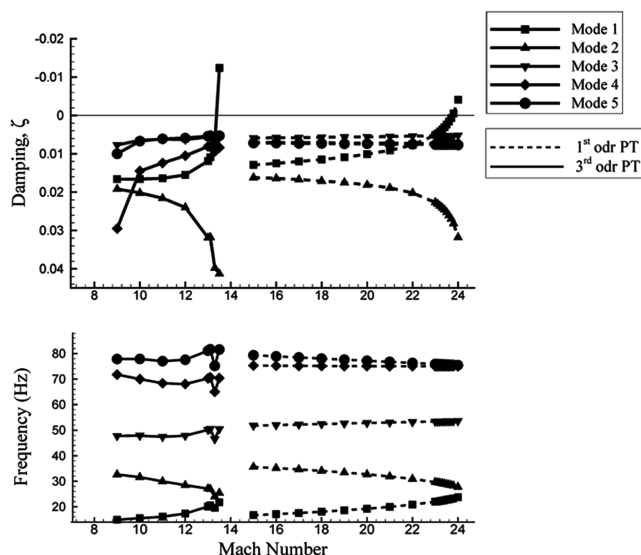
Fig. 9 Aeroelastic behavior of the low-aspect-ratio wing using first- and third-order piston theory aerodynamics at 40,000 ft.

mesh is a challenging task for three-dimensional configurations because the grid resolution required for accurate flow computations often places an excessive burden on computational resources. Therefore, it is necessary to consider the optimal distribution of cells around a body to obtain accurate flow predictions at reasonable computational costs.

Consider a steady hypersonic flow around the low-aspect-ratio wing shown in Fig. 3. At small angles of attack, an attached oblique shock will form at the leading and trailing edges of the wing, whereas an expansion fan is present at midchord. For inviscid flow, the surface pressure is a step function, with a discontinuity at midchord. To determine the best distribution of cells around the wing, four different grids were constructed with different computational domains and cell spacing. The root-section planes of each grid (mesh 1, mesh 2, mesh 3, and mesh 4) are shown in Fig. 10, and the complete computational domains of mesh 1 and mesh 4 are shown in Fig. 11. Note that meshes 2–4 have the same computational domain and grid resolution (0.63×10^6 cells); however, the cell spacing normal to the wing surface is varied, as shown. Also note that mesh 1 occupies a larger domain around the wing than meshes 2–4 and has a much higher grid resolution (4.0×10^6 cells). As illustrated in Fig. 10, the outer boundary of meshes 2–4 surrounding the leading surface of the wing (leading edge to midchord) was set at a distance 10% beyond the shock that forms at $M = 5.0$. This Mach number was chosen as an upper bound of the computational domain for the leading portion of the wing because it was unlikely that aeroelastic calculations would be performed below $M = 5.0$.

The inviscid pressure distribution for each test case at a cross section located at 75% span of the wing is shown in Fig. 12 for both a moderate ($M = 5.0$) and high ($M = 16.0$) Mach number. The importance of the mesh used in the flow calculations is clearly illustrated. As stated previously, the pressure at a cross section of the wing should be a step function with the pressure constant from the leading edge to midchord and from midchord to the trailing edge, with the discontinuity at midchord. As evident from Fig. 12, the surface pressure predicted using mesh 1 is nonuniform in the forward and aft sections. This indicates that neither the shock nor the expansion fan is captured well, and the discontinuity in pressure is distributed over a large number of streamwise grid points. Furthermore, although meshes 2–4 all capture the leading-edge shock, only mesh 4 correctly simulates a sharp change in pressure at midchord. This is particularly evident at $M = 16.0$. Finally, a comparison of Figs. 13a and 13b illustrates the efficiency of the smaller computational domain at high Mach number. Most of the fluid cells in mesh 4 are within the domain of influence of the flow, whereas many of the cells in mesh 1 are outside the domain of influence. Based on these results, mesh 4 was selected from among the four grids because it produced an accurate representation of the flow characteristics around the wing.

To complete the grid analysis, a flow convergence study was performed on mesh 4 using four additional grid resolutions (two coarser and two finer). Table 2 illustrates the effect of increasing grid resolution on the inviscid C_L and C_M for the low-aspect-ratio wing at $\alpha_s = 1$ deg. It is clear that the inviscid lift and moment coefficients are converged for the grid resolutions considered, because the maximum percent difference relative to the finest grid is just over 3%.

The L_2 and L_∞ norms of the error in p/p_∞ (relative to the finest mesh) are listed in Table 3. Typically, in a mesh-convergence study, the goal is to see these error norms decrease as the grid gets finer, to an order of magnitude of fractions of a percent. The results show that this goal is difficult to attain in discontinuous flows, because the discrete error norms are dominated by the fact that the shock location and thickness, when slightly different on the current mesh and finest mesh, lead to an $\mathcal{O}(1)$ error norm. In contrast, the lift and moment are less sensitive to exact locations of the discontinuities, because they are integral functions of the pressure. Therefore, the C_L and C_M calculations are selected in this case as the best indicators of convergence. Furthermore, it is appropriate to check the convergence of C_M in the context of the current study, because the torsional moment is an important factor in aeroelastic stability boundary computations.

a) Root plane of mesh 1   b) Root plane of mesh 2

c) Root plane of mesh 3   d) Root plane of mesh 4
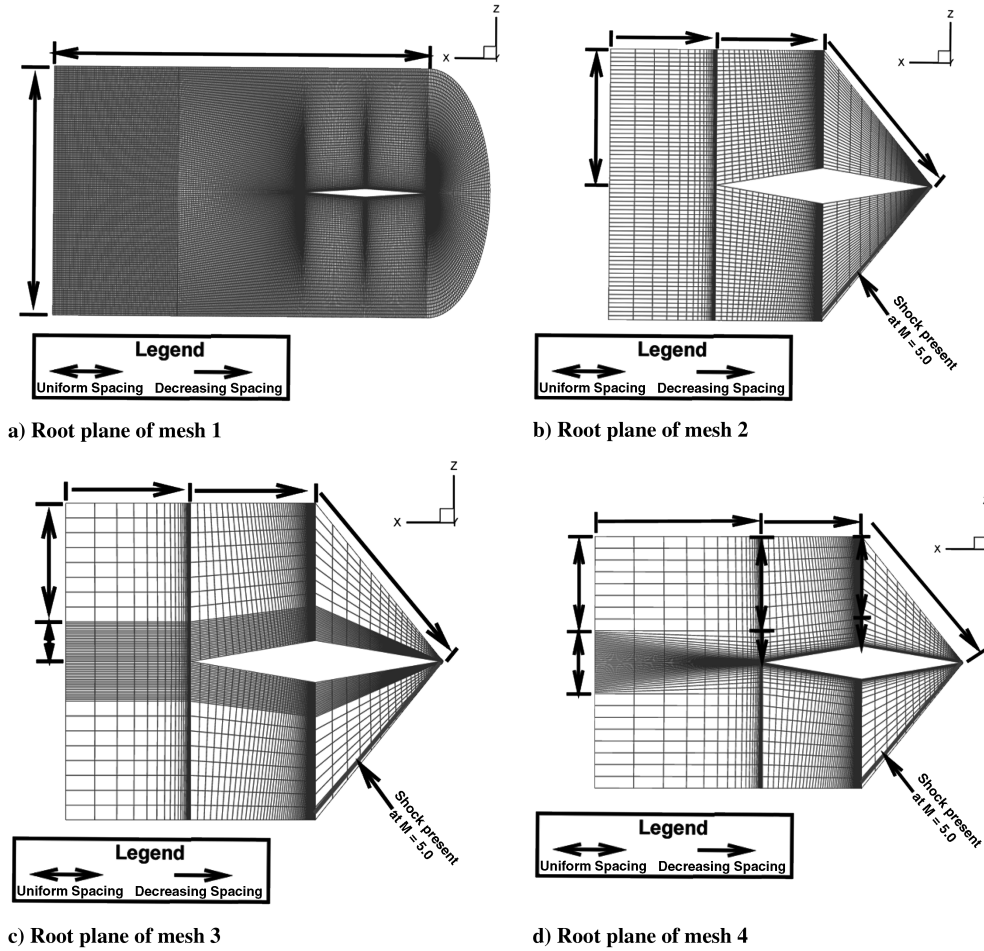
Fig. 10   Comparison of several different types of hypersonic mesh configurations. Two-sided arrows designate a region of uniform spacing, and one-sided arrows indicate a direction of decreasing cell spacing.

Because the majority of grid points in mesh 4 are clustered near the wing surface and boundary layers in hypersonic flows are relatively thick [1,68], this grid is also appropriate for Navier–Stokes computations. Convergence of the flow solutions with increasing grid resolution was also investigated using Navier–Stokes aerodynamics. The results of this study for C_L, C_M, and C_D are presented in Table 4. It is evident that the lift and moment coefficients are still relatively insensitive to the grid resolutions, because there is only a maximum difference of 7% relative to the finest grid. However, the drag coefficient requires significant grid refinement to

converge to within 10% of the finest-mesh result. The effect of inaccuracies in the force coefficients on the aeroelastic behavior of the wing and their sensitivity to grid resolution is also considered in the next section. The flow pattern at the 75% span station of the wing, generated by solving the Navier–Stokes equations on mesh 4 with 0.63×10^6 cells, is illustrated in Fig. 13c. Table 5 lists the L_2 and L_∞ norms of the Navier–Stokes-generated pressure for each grid. Similar to the inviscid case, the L_2 and L_∞ norms are large, due to the discontinuous nature of the flow. Again, the force coefficients are deemed to be better indicators of convergence.
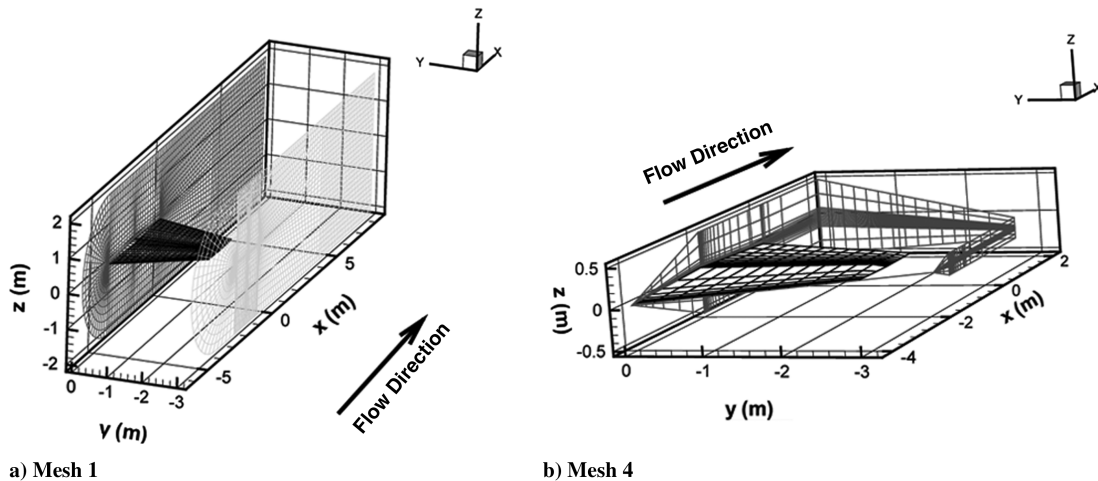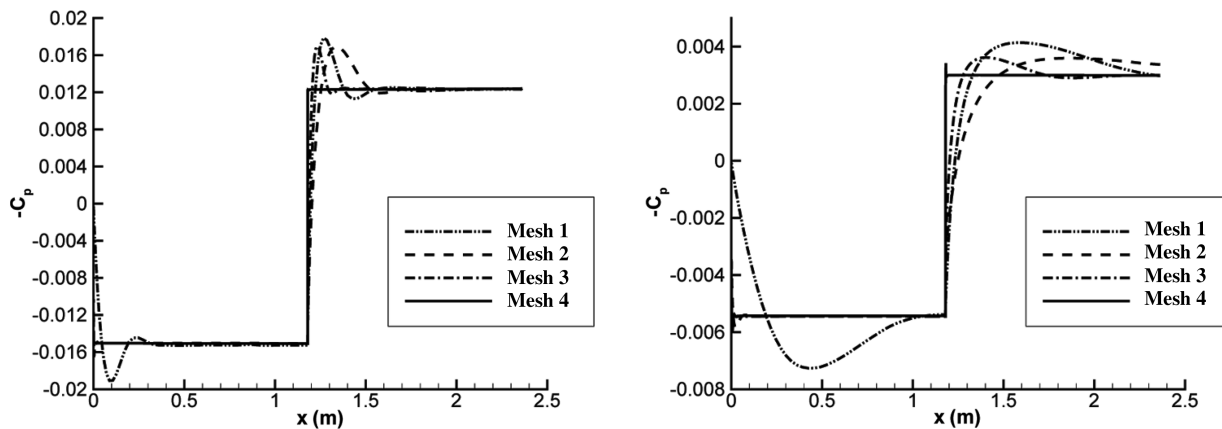

a) Mesh 1   b) Mesh 4

Fig. 11   Computational domains of two different mesh configurations.

a) Mach 5, 40,000 ft

b) Mach 16, 40,000 ft

Fig. 12 Values of C_p from 4 different grids using Euler aerodynamics, for a section located at the 75% span of the low-aspect-ratio wing.

a) Mesh 1, Euler aerodynamics

b) Mesh 4, Euler aerodynamics

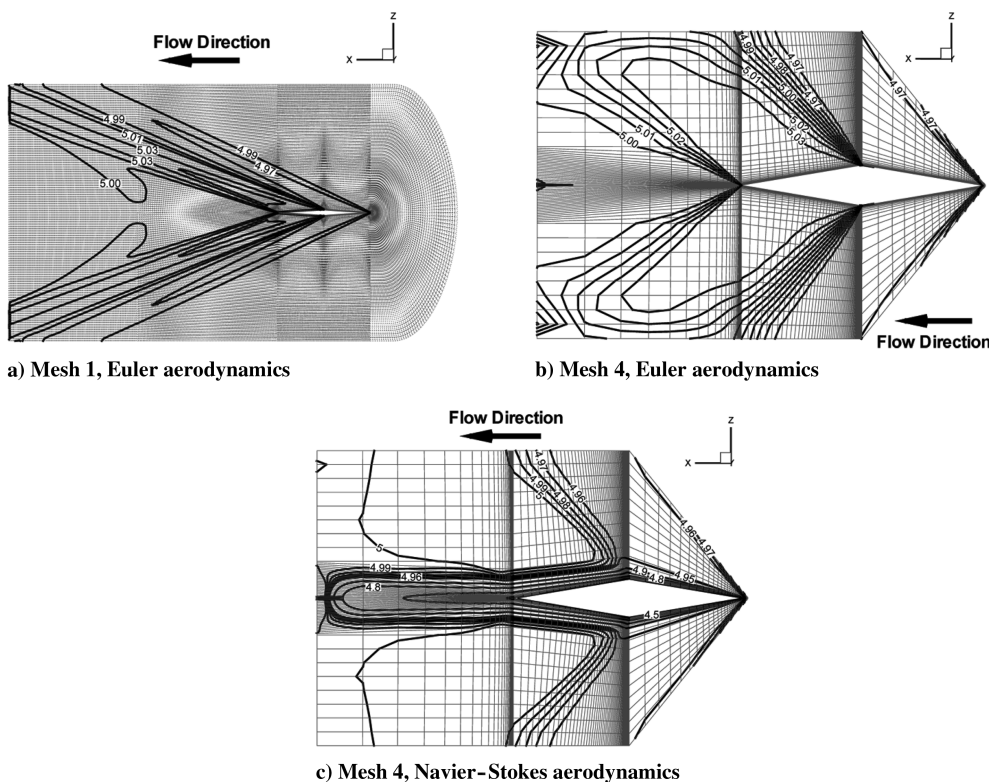c) Mesh 4, Navier–Stokes aerodynamics

Fig. 13 Mach contours of the flow at a section located at 75% span of a low-aspect-ratio wing; $M = 5.0$, 40,000 ft. Note that the z dimension is scaled.

Based on the grid convergence results presented in this section, mesh 4 is selected for aeroelastic computations on the low-aspect-ratio wing. With 0.63×10^6 cells, this grid is a $57 \times 353 \times 33$ C-H grid with 353 points around the wing and its wake (289 points on the wing surface), 57 points extending spanwise from the root (49 points on the wing on the wing surface), and 33 points extending radially

outward from the surface. Figure 11b illustrates the computational domain for this mesh. The root-section plane of the computational domain, shown in Fig. 10d, extends one-half root chord lengths downstream. The boundary of the grid surrounding the wing from the leading edge to midchord extends to a distance 10% beyond the shock that forms at $M = 5.0$. The computational domain in the

Table 2   Effect of grid resolution on the accuracy of C_L and C_M computations using Euler aerodynamics

| | C_L | | C_M | |
No. of cells	$M = 5.0$	$M = 16.0$	$M = 5.0$	$M = 16.0$
0.08×10^6	0.70%	3.09%	1.84%	3.16%
0.27×10^6	0.74%	1.53%	0.96%	1.84%
0.63×10^6	0.67%	1.11%	0.10%	1.29%
2.1×10^6	0.23%	0.44%	0.24%	0.43%
5.1×10^6	N/A	N/A	N/A	N/A

Table 3 L_2 and L_∞ norms of $\frac{p}{p_\infty}$ at various grid resolutions using Euler aerodynamics

| | L_2 | | L_∞ | |
No. of cells	$M = 5.0$	$M = 16.0$	$M = 5.0$	$M = 16.0$
0.08×10^6	0.1406	0.9047	0.3431	2.0672
0.27×10^6	0.0713	0.3930	0.1315	0.8004
0.63×10^6	0.0784	0.6342	0.2715	1.9873
2.1×10^6	0.0734	0.3838	0.1423	0.7716
5.1×10^6	N/A	N/A	N/A	N/A

Table 4   Effect of grid resolution on the accuracy of C_L, C_M, and C_D computations using Navier–Stokes aerodynamics

| No. of Cells | C_L | | C_M | | C_D | |
	$M = 5.0$	$M = 16.0$	$M = 5.0$	$M = 16.0$	$M = 5.0$	$M = 16.0$
0.08×10^6	0.82%	6.96%	7.15%	4.44%	21.75%	96.23%
0.27×10^6	1.28%	4.41%	6.23%	4.86%	15.30%	51.11%
0.63×10^6	1.14%	3.85%	5.53%	3.85%	11.48%	24.96%
2.1×10^6	0.29%	1.44%	0.32%	1.44%	2.05%	8.76%
5.1×10^6	N/A	N/A	N/A	N/A	N/A	N/A

Table 5 L_2 and L_∞ norms of p/p_∞ at various grid resolutions using Navier–Stokes aerodynamics

| No. of cells | L_2 | | L_∞ | |
	$M = 5.0$	$M = 16.0$	$M = 5.0$	$M = 16.0$
0.08×10^6	0.6128	7.0045	1.2862	15.3114
0.27×10^6	0.3794	2.6719	1.004	8.9927
0.63×10^6	0.5829	7.0423	1.2820	15.4131
2.1×10^6	0.3224	2.2489	0.9265	8.9043
5.1×10^6	N/A	N/A	N/A	N/A

spanwise direction also extends beyond the tip of the wing by 35% of the semispan length. Furthermore, the grid is tapered in all three dimensions to match the geometric taper of the wing.

It is important to mention that the current outer boundary for the grid is only useful for 0-deg angle-of-attack cases. For nonzero angle-of-attack aeroelastic analysis, the outer boundary of the grid must be moved appropriately to accommodate aeroelastic steady-state deflections of the wing.

C.   Aeroelastic Behavior of the Wing Using Euler and Navier–Stokes Aerodynamics

The ability to generate CFD-based aeroelastic results in the hypersonic flow regime represents a significant milestone toward the design of hypersonic vehicles. However, because this type of analysis is far from routine, a systematic study of several fundamental issues is important. Thus, several basic issues such as the setting of temporal input parameters for efficient time-accurate CFD calculations, as well as the effects of grid resolution, viscosity, and altitude on the aeroelastic behavior of the wing are examined in this section.

In addition to the global time-step input required for aeroelastic analysis in CFL3D, additional temporal parameters are necessary for a local pseudo-time-stepping scheme [32], which reduces linearization and factorization errors in the time-accurate flow computations. Such a scheme is implemented by specifying the number of subiterations as well as a pseudo-time-step size that is set in CFL3D by the input parameter CFL_τ. In general, decreasing the global time step reduces the number of subiterations required to achieve an accurate result, whereas increasing the grid refinement increases the number of subiterations required [32].

The effect of subiterations and CFL_τ on the hypersonic aeroelastic behavior of the low-aspect-ratio wing is illustrated in Fig. 14 using a 0.63×10^6 cell grid. These results were generated at 40,000 ft for $M_\infty = 12.0$ using Euler aerodynamics. Note that this velocity–altitude combination is impractical for a hypersonic vehicle and was used only for a trend-type study. This Mach number and altitude were chosen because it was expected, based on the preliminary analysis using piston theory, to result in aeroelastic behavior that was relatively close to, but not above, the flutter boundary. It is evident from Fig. 14 that the number of subiterations used has an effect on the aeroelastic behavior of the wing. Although the frequencies of all the modes remain constant, the damping varies with increasing subiterations. In particular, the first and second modes are substantially affected by the number of subiterations. The most significant impact is the relative magnitude of the damping, in which the first and second modes cross each other, depending on the

number of subiterations used. For $CFL_\tau = 1.0$, the damping of the second mode is greater than the damping of the first mode, based on 25–45 subiterations. Furthermore, the damping of all the modes remains almost constant in this range of subiterations. Also, when $CFL_\tau = 5.0$, which represents a larger step in pseudotime per subiteration, the same behavior is observed, but for a smaller number of subiterations. In the $CFL_\tau = 5.0$ case, when the number of subiterations varies between 20–35, the behavior is relatively unchanged. Based on these results, $CFL_\tau = 5.0$ with 20 subiterations is selected for Euler computations, because this combination provides accurate results that can be obtained with computational efficiency.

The aeroelastic behavior of the wing generated with Euler aerodynamics is presented in Fig. 15 for two different grid resolutions. The flutter Mach number is $M_f = 13.7$ ($0.15 < k_\omega < 0.49$) and $M_f = 13.8$ ($0.15 < k_\omega < 0.51$) for the 0.63×10^6 and 0.27×10^6 cell grids, respectively. This result is only 2% higher than the flutter Mach number predicted using third-order piston theory. Also, similar to the piston theory results, there is a coalescence in frequency between the first bending (mode 1) and first torsion (mode 2) modes, and the damping of the first mode approaches zero. Furthermore, the same divergence of damping in the first two modes is observed as the flutter point is approached. Also, similar to the piston theory results, the damping and frequency behavior in the higher modes (modes 3–5) is relatively constant as the Mach number is increased. Finally, it is evident that coarsening the mesh by almost 60% does not significantly alter the flutter boundary at this altitude. However, it is important to note that when the flutter Mach number is increased, such as due to an increase in altitude, the shock will lie closer to the surface of the wing. Therefore, as the shock approaches the surface, grid resolution may become significant because the number of the points in the shock layer decreases.

To determine the effect of viscosity on the aeroelastic behavior of the wing, the procedure is repeated using Navier–Stokes aerodynamics. First, the effect of increasing subiterations is shown
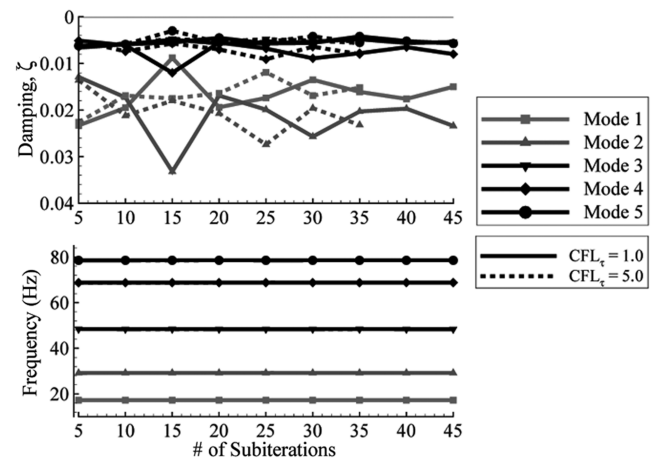
Fig. 14   Effect of increasing subiterations and CFL_τ on the aeroelastic behavior of the low-aspect-ratio wing using Euler aerodynamics at 40,000 ft. Symbols indicate the mode number, and the solid vs dashed lines indicate the value of CFL_τ.

a) Effect of increasing subiterations
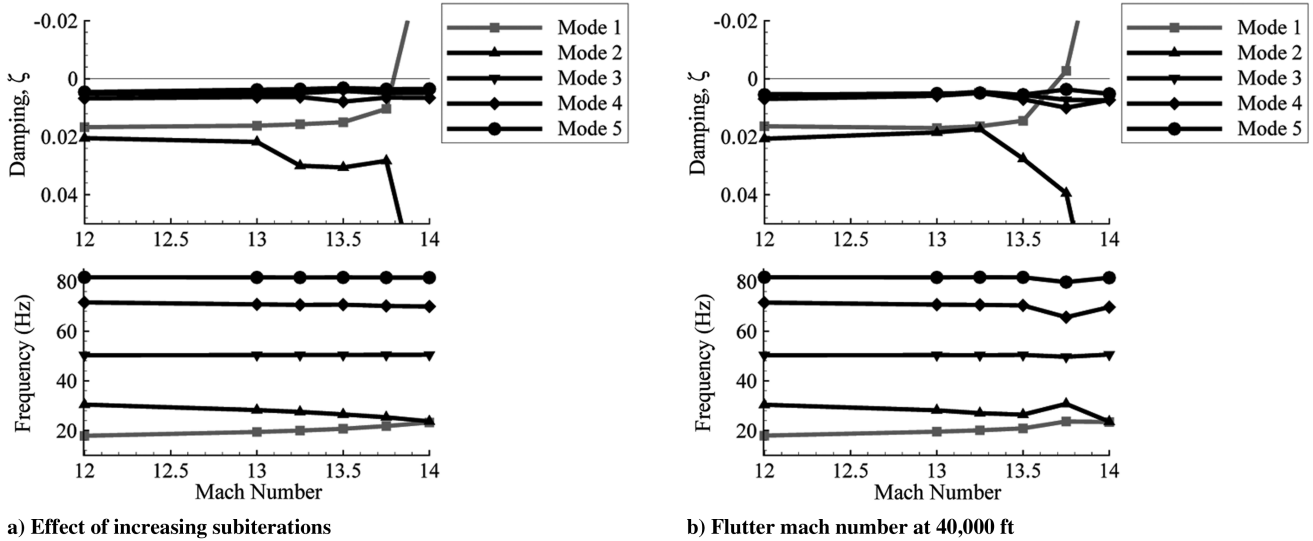
b) Flutter mach number at 40,000 ft

Fig. 15   Aeroelastic behavior of the low-aspect-ratio wing using Euler aerodynamics at 40,000 ft.

in Fig. 16a. It is apparent that in this case, with $CFL_\tau = 5.0$, at least 50 subiterations are required when computing Navier–Stokes aerodynamics.

The aeroelastic behavior of the wing computed using Navier–Stokes aerodynamics is illustrated in Fig. 16b. In this case, $M_f = 13.65$ ($0.14 < k_\omega < 0.50$), which is less than 1% lower than that predicted using Euler aerodynamics and is 1.5% higher than that predicted using third-order piston theory. As with the piston theory and Euler results, there is a coalescence in frequency and a divergence in damping of the first two modes as the flutter Mach number is approached. Again, the behavior in the higher modes is similar, with little change in the damping and frequencies as the Mach number is increased. A notable difference between these results and the inviscid results is the gradual approach of the first mode to zero damping. Both the piston theory and Euler results exhibited a more sudden change in damping at the flutter Mach number. Note that the Reynolds number for these computations is approximately $Re \approx 3 \times 10^8$ for the Mach numbers considered. Furthermore, note from Table 6 that the average y^+ values for the first grid point from the surface of the wing are $y^+ \leq 2.5$ for Mach numbers near the flutter boundary, which implies that the grid resolution within the boundary layer is adequate for these computations.

Finally, it is important to consider the value of reduced frequencies associated with the hypersonic aeroelastic problem. Comparison of

the reduced frequencies k_ω at flutter indicates that regardless of the aerodynamic model used, the reduced frequencies are invariably small in hypersonic flow. This partially explains the good agreement between the Euler/Navier–Stokes results and the piston theory results, because low reduced frequencies imply that quasi-steady aerodynamics, as represented by piston theory, may be appropriate.

D.   Flutter Boundary of the Low-Aspect-Ratio Wing

Next, the effect of increasing altitude on the flutter boundary in hypersonic flow is examined using the same method that was used for the height of 40,000 ft. This is shown in Fig. 17 for third-order piston theory and Euler and Navier–Stokes aerodynamics. The results labeled "baseline grid" correspond to a 0.63×10^6 cell grid, and those labeled "fine grid" correspond to a 2.1×10^6 cell grid.

Several interesting observations can be made based on these results. First, it is evident that there are minor differences between the flutter boundaries calculated using third-order piston theory and Euler aerodynamics at all altitudes considered. Specifically, there is less than 5% difference between the flutter Mach number and less than 8% difference between dynamic pressure at flutter for all altitudes considered. At 60,000 ft, however, the Euler results generated using the baseline grid begin to diverge due to lack of grid resolution within the shock layer as the Mach number increases and the shock moves close to the wing surface [69].
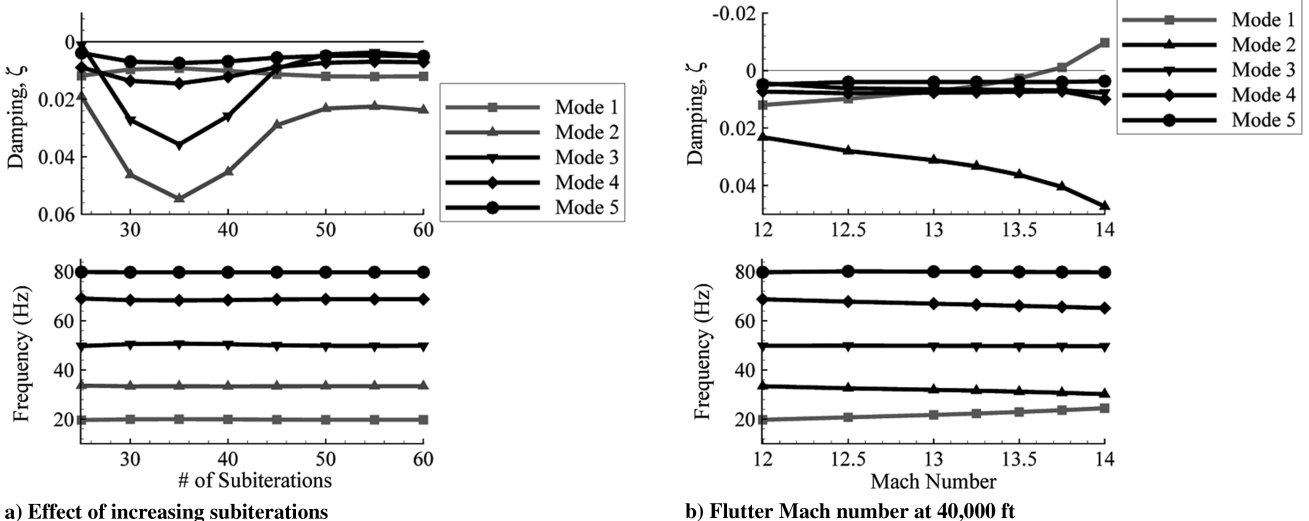

a) Effect of increasing subiterations

b) Flutter Mach number at 40,000 ft

Fig. 16   Aeroelastic behavior of the low-aspect-ratio wing using Navier–Stokes aerodynamics at 40,000 ft, $CFL_\tau = 5.0$.

Table 6 Average y^+ values for the first grid point from the wing surface at Mach numbers near the flutter boundary ($M_f = 13.65$ at 40,000 ft) obtained using Navier–Stokes aerodynamics

Avg. y^+	M_∞
2.50	12.0
2.37	12.5
2.34	13.0
2.30	13.5
2.27	14.0

In general, there is good agreement between the stability boundaries generated using inviscid and Navier–Stokes aerodynamics from 40,000–70,000 ft. In this range of altitudes, there is less than 8% difference in the flutter Mach number and less than 10% difference in dynamic pressure at flutter between the fine-grid Navier–Stokes and inviscid results. Note that as in the case of the stability boundary calculated using Euler aerodynamics, the Navier–Stokes results generated with the baseline grid begin to diverge from the fine-grid results at 50,000–60,000 ft. Note that results were not generated above 70,000 ft, due to the excessive Mach numbers required to generate flutter.

An interesting result is the large differences between the viscous and inviscid results at 30,000 ft and lower. In this region, the differences in flutter Mach number and dynamic pressure grow to nearly 20 and 60%, respectively, between the inviscid and viscous results. This can be partially explained, however, by comparing plots of the steady pressure coefficient, illustrated in Fig. 18. It is evident that the displacement thickness is substantial for this configuration at the lower altitudes. At 20,000 feet and $M_\infty = 5.0$, there is a significant increase in the viscous pressure coefficient over the forward surface of the wing compared with the inviscid result. This is also true for $M_\infty = 9.0$ at 30,000 ft; however, in this case, the baseline grid does not capture the boundary-layer effects over the forward portion of the wing. When the altitude is increased to 40,000 ft, there is only a small difference between the inviscid and viscous steady pressure coefficient at $M_\infty = 13.5$. Despite these interesting results, it is apparent that at moderate-to-high altitude and Mach numbers (where hypersonic vehicles typically operate), viscous effects are not important for the three-dimensional configuration considered.

The CFL3D parameters used to obtain these results are listed in Table 7. Note that for $M_\infty < 5.0$, the outer boundaries of the grid were expanded to accommodate flows with freestream Mach numbers of $M_\infty \geq 2.0$. Furthermore, note that to compute the unsteady Navier–Stokes aerodynamics on the fine grid, the original time step was reduced by a factor of 2.
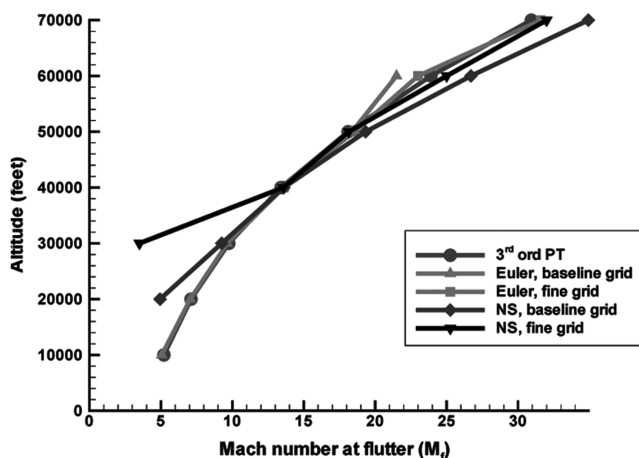
### E. Aerothermoelastic Behavior of a Three-Dimensional Low-Aspect-Ratio Wing

As shown in the previous section, the low-aspect-ratio wing flutters at impractical Mach numbers for the altitudes considered when aerodynamic heating is ignored. In this section, the effect of aerodynamic heating is combined with the aeroelastic analysis of the low-aspect-ratio wing using the refined aerothermoelastic procedure discussed in Sec. II.G.

The low-aspect-ratio cantilevered wing is an appropriate example for studying the effects of aerodynamic heating on an aeroelastic system, because the restrained warping at the root of the wing induces thermal stresses, which in turn affect the torsional stiffness of the wing [13,14,64–66,70] and modify its frequencies and mode shapes. The effect of warping restraint increases as the aspect ratio of a structure diminishes [71]. Early studies of this effect [72] indicate that by modeling a low-aspect-ratio wing as a plate, the effect of warping restraint is inherently included. More recently, this effect has been studied in the context of composites [73,74]. In these studies, it has been pointed out that warping restraint is not only important for low-aspect-ratio metallic structures, but also for composite structures in which the material proprieties are nonisotropic. Furthermore, it was shown that the warping stiffness of a cantilever plate is a function of both aspect ratio and the ratio of bending/torsion stiffness [12,73]. This observation is important for hypersonic vehicles in which structural properties are altered by aerodynamic heating.

Note that the aerothermodynamic quantities in this study were determined with a 2.1×10^6 cell grid using CFL3D to solve the Navier–Stokes equations. The heat-transfer analysis was performed using the transient analysis solution (solution 159) [75] in MSC.Nastran with the heat option selected. The effect of thermal radiation was included. The heated modes and frequencies of the wing were determined using the nonlinear statics solution in MSC.Nastran (solution 106) [75] with the normal-modes option selected. As stated previously, the analysis includes both the effect of material-property degradations and thermal stresses.

1. Modified Structural Model for the Low-Aspect-Ratio Wing

Preliminary heated analysis of the wing revealed that it was prone to local-edge buckling along the leading and trailing edges, similar to that discussed in [76], for relatively small temperature increases. Therefore, the wing was modified for this study to reduce this susceptibility to local-edge thermal buckling. The leading and trailing edges were stiffened and several spars and ribs were added throughout the entire wing. These modifications introduced minor (less than 10%) changes in the structural mass and first two free-vibration frequencies, as illustrated in Table 8. Comparing the mode shapes of the modified wing shown in Fig. 19 with the original mode
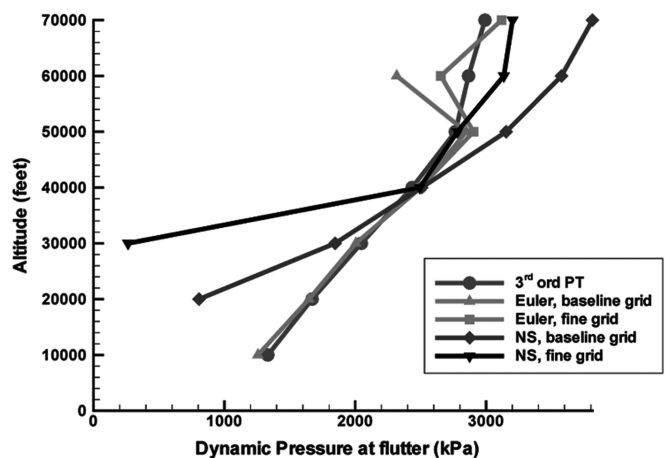
a) Mach number   b) Dynamic pressure

Fig. 17 Flutter envelope of the low-aspect-ratio wing, calculated using third-order piston theory, Euler and Navier–Stokes aerodynamics (PT denotes piston theory).

a) $M = 5.0$, $Re = 2.62 \times 10^8$, 20,000 ft

b) $M = 9.0$, $Re = 3.42 \times 10^8$, 30,000 ft

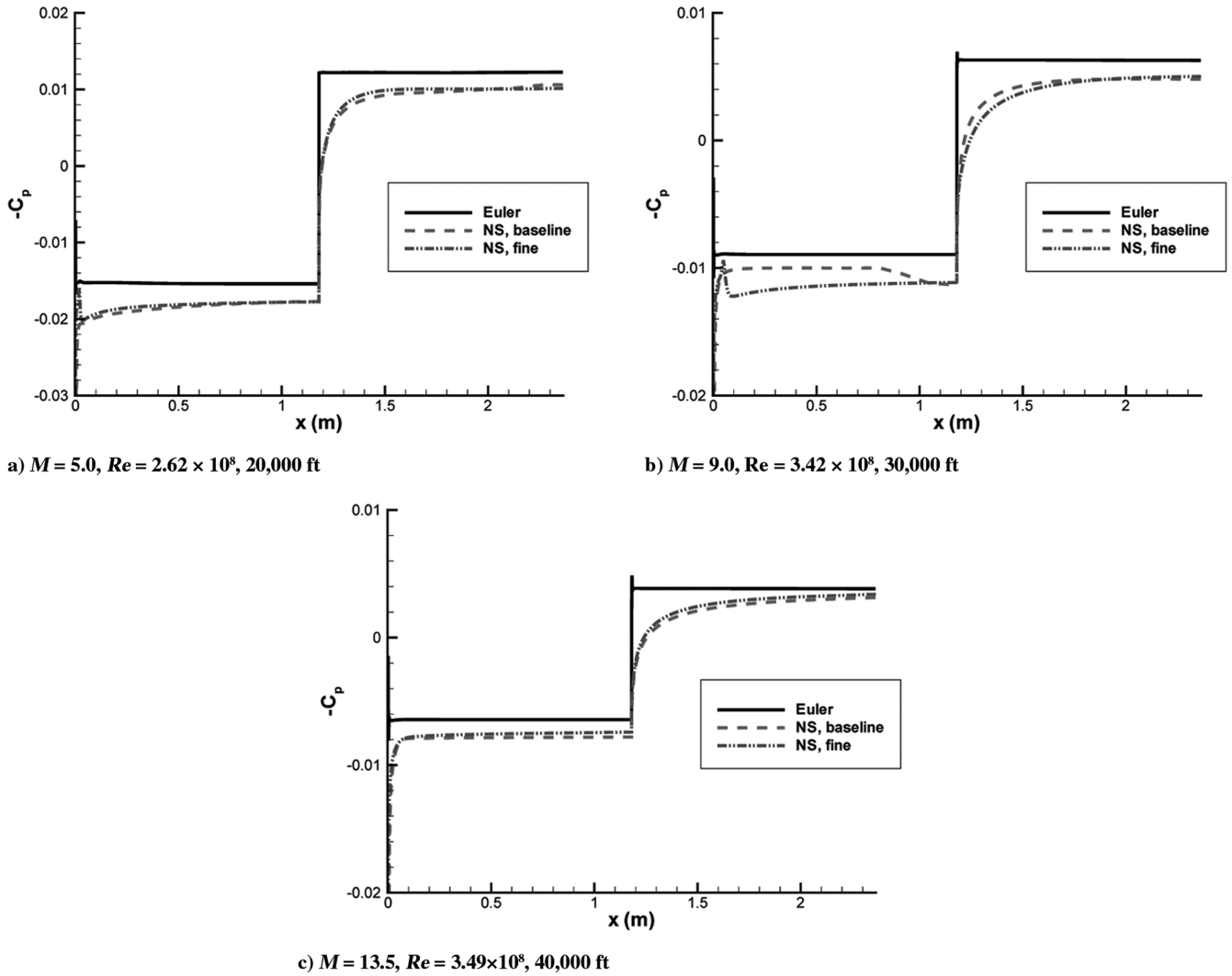c) $M = 13.5$, $Re = 3.49 \times 10^8$, 40,000 ft

Fig. 18 Comparison of the steady pressure coefficient on a low-aspect-ratio wing at the 75% span location, using Euler and Navier–Stokes (NS) aerodynamics, for several different operating conditions.

shapes shown in Fig. 5 shows that only the fourth mode shape has changed significantly. The fourth mode shape of the original wing is an antisymmetric bending mode, and for the modified wing, it is a symmetric bending mode.

The effect of material-property degradations is accounted for by changes in the modulus of elasticity and thermal expansion coefficient with temperature. Experimental measurements on metals indicate that the modulus of elasticity decreases more rapidly for static measurements when compared with dynamic measurements [14]. Reference [77] suggests that this difference is due to several internal-friction mechanisms, among which anelastic effects appear to be predominant. Data on the dynamic modulus of elasticity for

various alloys, including 2024-T3 aluminum alloy used in this study, at different temperatures were taken from [77]. Data on the thermal expansion coefficient for 2024-T3 aluminum alloy were found in [78].

2.   Thermal Protection System for the Low-Aspect-Ratio Wing

Because the low-aspect-ratio wing is constructed from aluminum, it is combined with a thermal protection system (TPS) to delay the high-temperature environment of hypersonic flow from exceeding material limits. The TPS selected is based on [79]. It consists of a 0.45-mm René 41® metal heat shield and a 3.8-mm flexible Min-K®

Table 7   CFL3D parameters for 3-D Euler and Navier–Stokes aeroelastic calculations; computational time is for Athlon 2000MP CPUs

Parameter	Euler, baseline	Euler, fine	N-S, baseline	N-S, fine
No. subiterations	20	35	50	45
CFL_τ	5.0	5.0	5.0	5.0
Δt (s)	0.25×10^{-3}	0.25×10^{-3}	0.25×10^{-3}	0.12×10^{-3}
No. of time steps	500	500	500	1000
Grid configuration	mesh 4	mesh 4	mesh 4	mesh 4
Wall type	N/A	N/A	Adiabatic	Adiabatic
Turbulence model	N/A	N/A	Spalart–Allmaras	Spalart–Allmaras
No. of cells	0.63×10^6	2.1×10^6	0.63×10^6	2.1×10^6
No. processors	12	16	12	31
Computation time, h	6.5	20	16.5	30

Table 8   Comparison of the original and modified low-aspect-ratio wings

Parameter	Original Wing	Modified Wing	% Diff
Wing Mass, kg	350.05	377.73	8%
Mode 1 freq., Hz	13.41	14.28	7%
Mode 2 freq., Hz	37.51	40.94	9%
Mode 3 freq., Hz	49.18	60.06	22%
Mode 4 freq., Hz	77.14	81.86	6%
Mode 5 freq., Hz	79.48	97.25	22%

thermal insulation blanket between the wing and heat shield. The René 41 heat shield can withstand temperatures up to approximately 1500 K and is assumed to have an emissivity $\epsilon = 0.85$.

3.   Effect of Aerodynamic Heating on the Free-Vibration Characteristics of the Wing

Figure 20a illustrates the effect of transient heating on the free-vibration frequencies of the modified wing at 100,000 ft for $M_\infty = 10.0$, 15.0, and 20.0 ($\alpha_s = 0$ deg). In each case, there is a reduction of the second, third, and fifth modal frequencies as the wing is heated. Also, there is a slight increase in the first and fourth modal frequencies, in which the fourth modal frequency switches order with the fifth modal frequency. In each case, the wing thermally buckles (as indicated by the sudden drop in frequency) after a specific duration: namely, 30, 18, and 13 min for $M_\infty = 10.0$, 15.0, and 20.0, respectively. Note that the change in frequencies due to aerodynamic heating is similar to that experienced by the solid plate structures studied in [65,66]. Specifically, the introduction of modal coupling and thermal buckling is due to the presence of thermal stresses [65,66].

It is interesting to note that each of the three results are qualitatively similar: each Mach number produces similar changes in frequency; the main difference in the results is the amount of time required for the changes to occur. This behavior is probably due to an increase in heating rate with increasing Mach number, whereas the temperature distribution remains relatively unchanged [67]. In Fig. 20b, the same results are presented; however, the frequencies are plotted as a function of a reference temperature T_{ref}. The reference temperature was arbitrarily chosen as the leading-edge temperature at the 75% span location. Note that there are only minimal differences in the three cases when the results are plotted as a function of this reference temperature. Figure 20b shows that at 100,000 ft, the wing is susceptible to buckling for 660 K < T_{ref} < 680 K, regardless of the Mach number.

In practice, control surfaces on hypersonic vehicles will be required to have a small angle of attack to produce the necessary control forces. It has been shown [80,81] that for the unheated case, a small angle of attack will not significantly modify the flutter boundary of a two-dimensional typical section. However, angle of attack is important when aerodynamic heating is considered, because it introduces asymmetry in the temperature distribution between the upper and lower surfaces of a wing. This in turn introduces thermal stresses not present in 0-deg angle-of-attack cases. The effect of angle of attack on the heated free-vibration frequencies of the modified wing is shown in Fig. 20c at 100,000 ft for $\alpha_s = 2$ deg and $M_\infty = 20$. It is clear that in the heated case, a small amount of angle of attack can significantly change the free-vibration frequencies of the wing. For this case, there is not a smooth change in frequency as the wing is heated, and the previous distinction as to where buckling occurs is eliminated. Furthermore, the frequencies are much lower in the presence of angle of attack for 600 K < T_{ref} < 665 K.

The maximum prebuckling changes in modal frequencies for the heated wing, for both the zero- and nonzero-angle-of-attack cases, are given in Table 9. It is apparent that aerodynamic heating results in up to 25–50% reduction in the modal frequencies of the wing.

4.   Aerothermoelastic Behavior of the Wing Along a Representative Hypersonic Trajectory

Although it is relevant to study the effect of aerodynamic heating on the free-vibration characteristics of the wing, the important issue is the effect of aerodynamic heating on the flutter boundary. The time-dependent operating conditions are important when studying the aerothermoelastic behavior of a hypersonic configuration. For instance, the transient heating of a wing at a constant altitude with constant Mach number is substantially different from the transient heating of a wing with continuously changing operating conditions. For a particular vehicle, the transient heating of the wing is inherently linked to its trajectory. Furthermore, as illustrated by Fig. 17, the flutter Mach number and dynamic pressure change significantly, depending on the operating altitude. Therefore, for an accurate aerothermoelastic study of a particular configuration, the trajectory is required. In this study, a representative hypersonic trajectory, based approximately on the DARPA/U.S. Air Force FALCON program, is used to examine the aerothermoelastic behavior of the low-aspect-ratio wing.

F.   Representative Hypersonic Trajectory

As mentioned earlier, the FALCON program is expected to provide the United States with a global prompt strike capability by using hypersonic suborbital launch platforms [5]. The long-term goal of FALCON is an autonomous hypersonic cruise vehicle (HCV) that will take off like a conventional aircraft and transport 12,000 lb of cargo up to 17,000 km in less than 2 h. The trajectory of the HCV consists of three phases. In the initial phase, the vehicle takes off from a conventional runway and climbs from sea level to 40 km, where the Mach number is a maximum at $M_\infty = 12$. In the second phase, the engines are turned off, however, the HCV continues to ascend ballistically to an apogee of 60 km. At this point, the vehicle begins an equilibrium glide to an altitude of 35 km. Here, the third phase
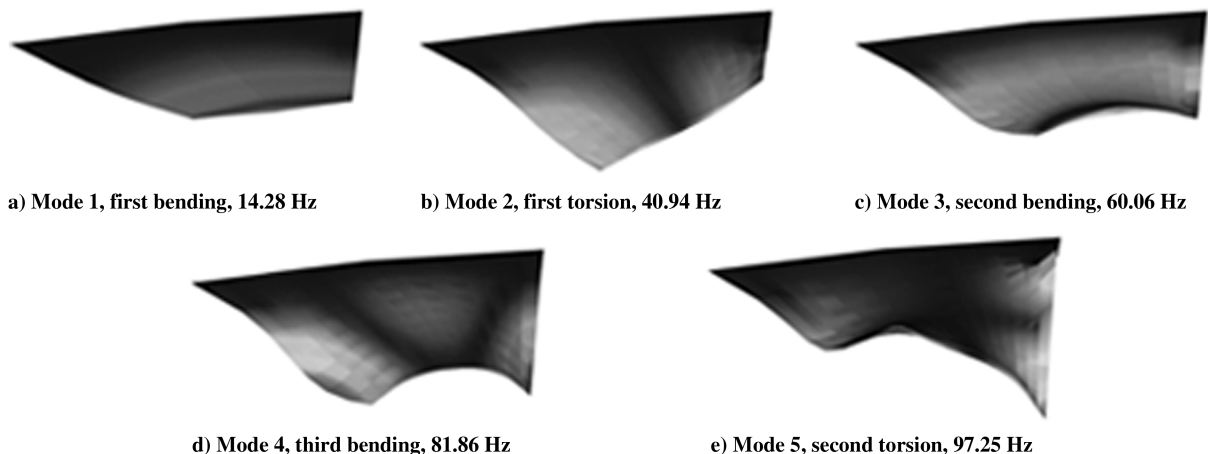

a) Mode 1, first bending, 14.28 Hz   b) Mode 2, first torsion, 40.94 Hz   c) Mode 3, second bending, 60.06 Hz

d) Mode 4, third bending, 81.86 Hz   e) Mode 5, second torsion, 97.25 Hz

Fig. 19   First 5 free-vibration modes of the modified low-aspect-ratio wing.

a) Variation of frequency vs time

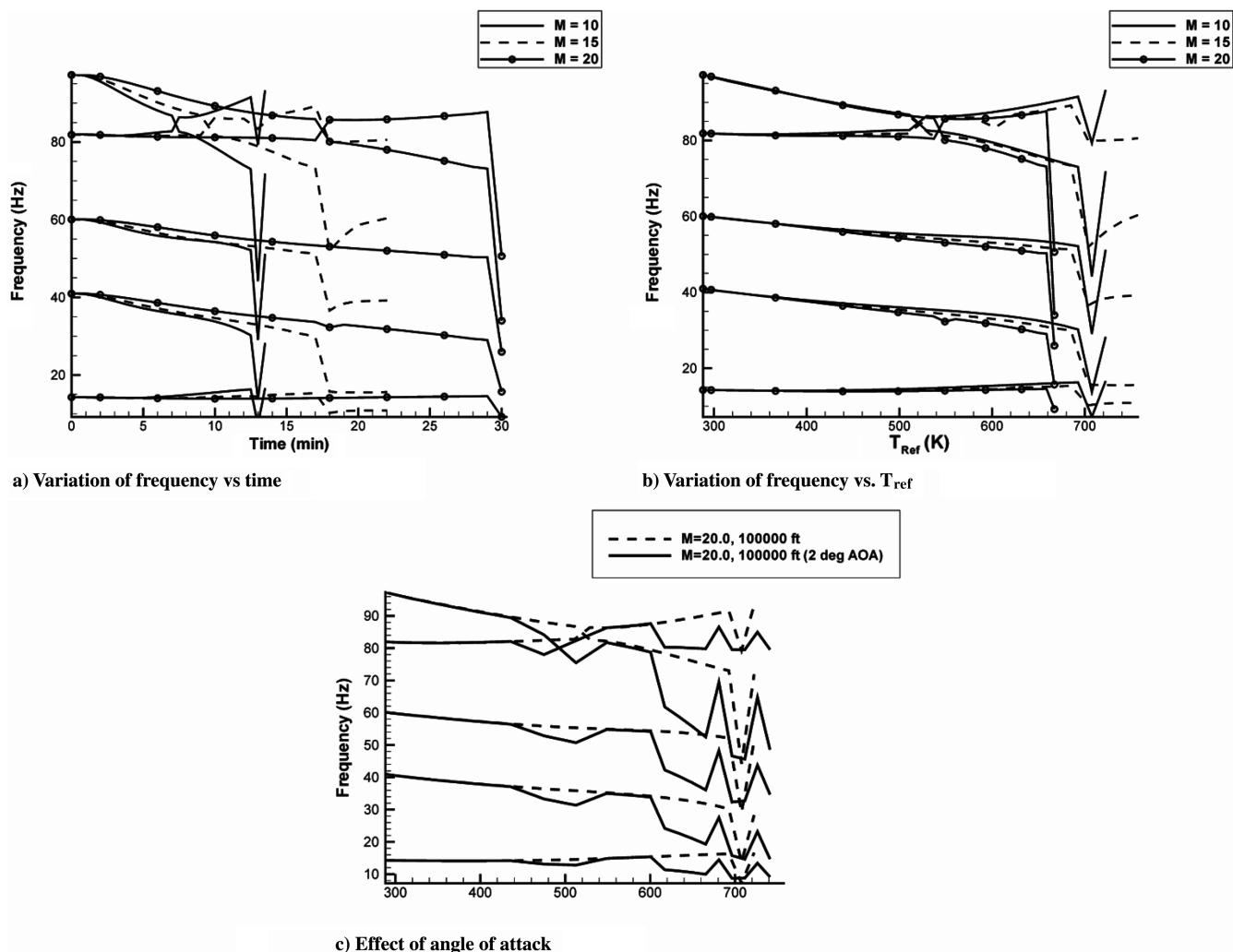b) Variation of frequency vs. T_{ref}

c) Effect of angle of attack

Fig. 20　Natural frequencies of the modified low-aspect-ratio wing subject to aerodynamic heating at 100,000 ft (AOA denotes angle of attack).

begins as the engines reignite and propel the vehicle back to an altitude of 40 km ($M_\infty = 12$) to start the second phase again. This skipping-type trajectory is proposed for the HCV to prevent heat buildup by operating in a near-space environment.

Using this description of the FALCON HCV trajectory, a representative hypersonic trajectory was formulated. For the initial phase, studies on the NASP [82,83] were used to extract typical trajectory data for an airbreathing ascent from a conventional runway. For the skip phase from 40 to 60 km, the change in altitude and Mach number is determined assuming simple ballistic motion for the vehicle. For the skip phase from 60 to 35 km, the trajectory is defined by an equilibrium glide [84], in which it is assumed that the HCV has an $L/D \approx 5.0$ [10]. For the third phase, or intermediate phase between skip portions, a linear acceleration is assumed from the end of the glide phase at 35 km to $M_\infty = 12$ at 40 km. This trajectory is shown in Fig. 21, in which the change in altitude, Mach number, and range are provided as a function of time. Note that this representative trajectory meets the stated mission objective of reaching a target distance of 17,000 km within 2 h.

To compute the transient heating of the wing and the subsequent changes in free-vibration characteristics, the aerodynamic heating

input in the FEA portion of the aerothermoelastic solution process, depicted in Fig. 8, was updated at 1-min intervals along the trajectory. Note that between each update, the aerodynamic heating boundary condition was assumed constant.

G.　Free-Vibration Characteristics of the Wing Along the Trajectory

Using the representative hypersonic trajectory, the variation in free-vibration characteristics of the wing was determined. To assess the sensitivity of the free-vibration characteristics to relatively small variations in the trajectory, two different cases were studied. First, the free-vibration characteristics were calculated along the trajectory for the wing at varying angles of attack: namely, $\alpha_s = 0$, 2, and 4 deg. The results from this analysis are presented in Fig. 22a. Qualitatively, these results are similar to the constant Mach number/altitude results presented earlier, as well as the behavior exhibited by nonuniformly heated solid plate structures [65,66]. There is a decrease in the second, third, and fifth modal frequencies and an increase in the fourth modal frequency. As before, the fourth and fifth modal frequencies switch order. The first modal frequency is practically unchanged along the trajectory. It is interesting that there is little

Table 9　Maximum percent change in the prebuckled modal frequencies of the heated low-aspect-ratio wing at an altitude of 100,000 ft (a negative sign indicates a decrease in frequency)

Case	Mode 1	Mode 2	Mode 3	Mode 4	Mode 5
$\alpha_s = 0$ deg, $M = 10.0$	2.1%	−29.2%	−16.3%	7.1%	−24.8%
$\alpha_s = 0$ deg, $M = 15.0$	7.4%	−26.9%	−14.6%	9.0%	−24.5%
$\alpha_s = 0$ deg, $M = 20.0$	14.1%	−26.2%	−13.2%	11.8%	−24.9%
$\alpha_s = 2$ deg, $M = 20.0$	−30.3%	−52.9%	−39.9%	−2.5%	−46.0%

variation between the modal frequencies calculated at different angles of attack, in contrast to the large differences observed for the constant Mach number/altitude case presented in Fig. 20c.

For the second case, the free-vibration characteristics of the wing are calculated along the trajectory with the Mach number increased by 25%, with $\alpha_s = 2$ deg. From Fig. 22b, it is evident that increasing the Mach number by 25% produces qualitatively similar results; however, the time to thermal buckling is reduced by approximately 8 min. Note that increasing the Mach number by 25% has a more substantial effect on the modal frequencies of the wing than increasing the angle of attack from 0 to 4 deg for this trajectory.

Figure 22c illustrates the change in frequencies along the trajectory as a function of the reference temperature T_{ref}. It is evident that when the frequencies are plotted as a function of reference temperature, there are only minimal differences between each case. Similar to the constant-Mach number/altitude cases, this implies that whereas the heating rate changes by varying the Mach number and angle of attack, the temperature distribution throughout the wing remains primarily constant [67].

The maximum prebuckling changes in modal frequencies along the hypersonic trajectory are presented in Table 10. The aerodynamic heating along the trajectory results in 20–30% reductions in the second, third, and fifth modal frequencies of the wing. In particular, the maximum reduction in stiffness occurs for the first torsional mode (second modal frequency), which is a critical mode for flutter. It is interesting that these results are quantitatively similar to the 0-deg angle-of-attack case presented in Table 9, even though several of the modal frequencies were computed at a nonzero angle of attack.

H. Flutter Boundary of the Wing Along the Trajectory

The time-dependent free-vibration characteristics calculated in the previous section are used to perform an aerothermoelastic analysis of the wing along the trajectory. In the previous sections, the aeroelastic behavior of the wing was calculated for varying Mach numbers and altitudes, and heating was neglected. Therefore, flutter was calculated by holding altitude constant and increasing Mach number until critical damping of the system occurred. In contrast, in an aerothermoelastic solution, the aerodynamic heating couples the structural properties to the operating conditions. Therefore, the structure must be updated according to the operating conditions at each current point on the trajectory. Subsequently, similar to the unheated case, flutter can be calculated by holding altitude constant and increasing the Mach number. However, it is important to emphasize that this is a virtual-flutter Mach number, because the structural properties are not updated at each increase in Mach number to the flutter point. Therefore, this procedure yields only a quantitative measure of the proximity to flutter, but not the actual flutter Mach number. Thus, it is important to check the sensitivity of the virtual-flutter Mach number to perturbations in the trajectory, such as modest increases to the trajectory operating Mach number.

An important issue with the current trajectory is the operation of the HCV at high altitudes. As illustrated in Fig. 17, the original wing flutters at very high Mach numbers and low altitudes, which are not representative of an actual hypersonic trajectory. The modified wing used for this aerothermoelastic study is stiffer than the original wing. It also operates at near-space altitudes along many portions of the trajectory, and therefore the virtual Mach numbers required to generate flutter for the wing are excessive. Thus, in the calculations performed in this section for each operating condition along the trajectory, the Mach number and altitude are held constant and only the dynamic pressure is increased until flutter is achieved. Using this method, the proximity to flutter can be determined by calculating the ratio of the virtual-flutter dynamic pressure q_{vf} to the freestream dynamic pressure q_∞. A value of unity for this ratio at a given point on the trajectory implies the wing will flutter.
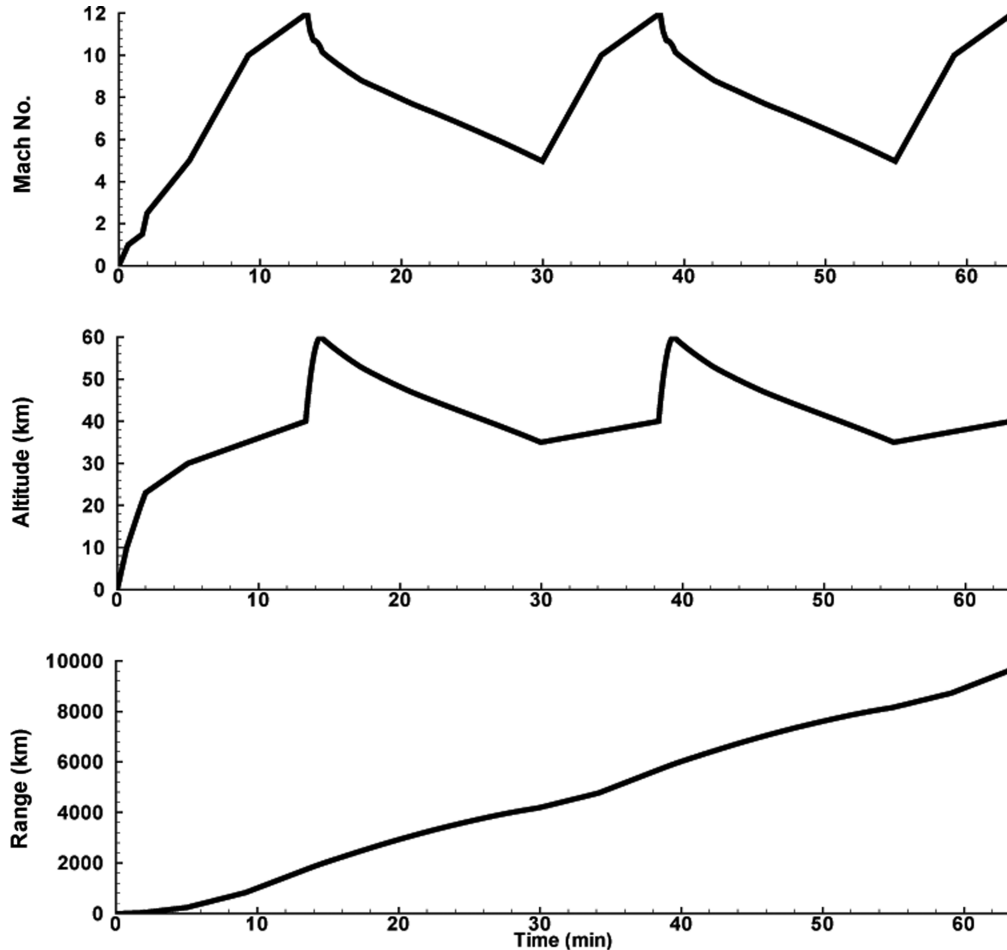

Fig. 21   Representative trajectory, based on the FALCON program, of a hypersonic vehicle.

The aerothermoelastic behavior of the wing along the trajectory is depicted in Fig. 23. Because of the proximity of the flutter boundaries predicted using third-order piston theory and CFD-based aerodynamics at high altitudes and Mach numbers, as shown in Fig. 17, it was decided to perform the majority of aerothermoelastic computations for the modified wing using third-order piston theory aerodynamics. However, for verification purposes, the aerothermoelastic behavior was also computed using Euler unsteady aerodynamics at a few points on the trajectory. Several interesting conclusions can be drawn from these results. By comparing the heated and unheated dynamic pressure ratios of the 0-deg angle-of-attack cases, it is evident that before thermal buckling, aerodynamic heating reduces the flutter margin by up to 40%. However, as expected, for most portions of the trajectory, the virtual-flutter dynamic pressure is significantly higher than the freestream dynamic pressure for the cases considered here. For the unheated case and first 30 minutes of the heated cases, the virtual-flutter dynamic pressure is 2 to 3 orders of magnitude higher than the freestream dynamic pressure. Furthermore, the minimum dynamic pressure ratios are approximately $\mathcal{O}(10)$. These minimum ratios occur after the first skip phase and during the reacceleration phase, in which the altitudes are relatively moderate and the Mach numbers are at their peak. It is also evident from these results that angle of attack does not significantly alter the flutter margin of the wing. Furthermore, increasing the Mach number by 25% results in an approximately 30% reduction in the dynamic pressure ratio in the prebuckled portion of the trajectory. Finally, note that as in the unheated case, there are only

minimal differences between the Euler and third-order piston theory results.

It is apparent from the large dynamic pressure ratios that for this type of trajectory, thermal buckling is more critical to the wing than flutter. This is likely due to the low-density air present at the near-space environment of the representative trajectory. These results emphasize the need for advanced materials and/or an active cooling system, because the wing fails well before the 17,000-km desired range of the HCV. For the trajectory selected, the wing buckles after approximately 7000 km (45 min).

IV. Conclusions

The presented studies in hypersonic aeroelasticity and aerothermoelasticity allow one to reach several useful conclusions:

1) For the low-aspect-ratio wing, the use of first-order piston theory aerodynamics in hypersonic flow results in unconservative flutter boundary predictions. This emphasizes the importance of configuration thickness in the hypersonic regime, because it is a second-order-or-higher effect.

2) In three-dimensional configurations, efficient distribution of the mesh points around the body is critical for optimal usage of computational resources. For hypersonic flow, grid refinement is required near the surface and in regions in which the flow changes direction.

3) The aeroelastic behavior of a system, predicted using time-accurate CFD solutions based on the Euler and Navier–Stokes
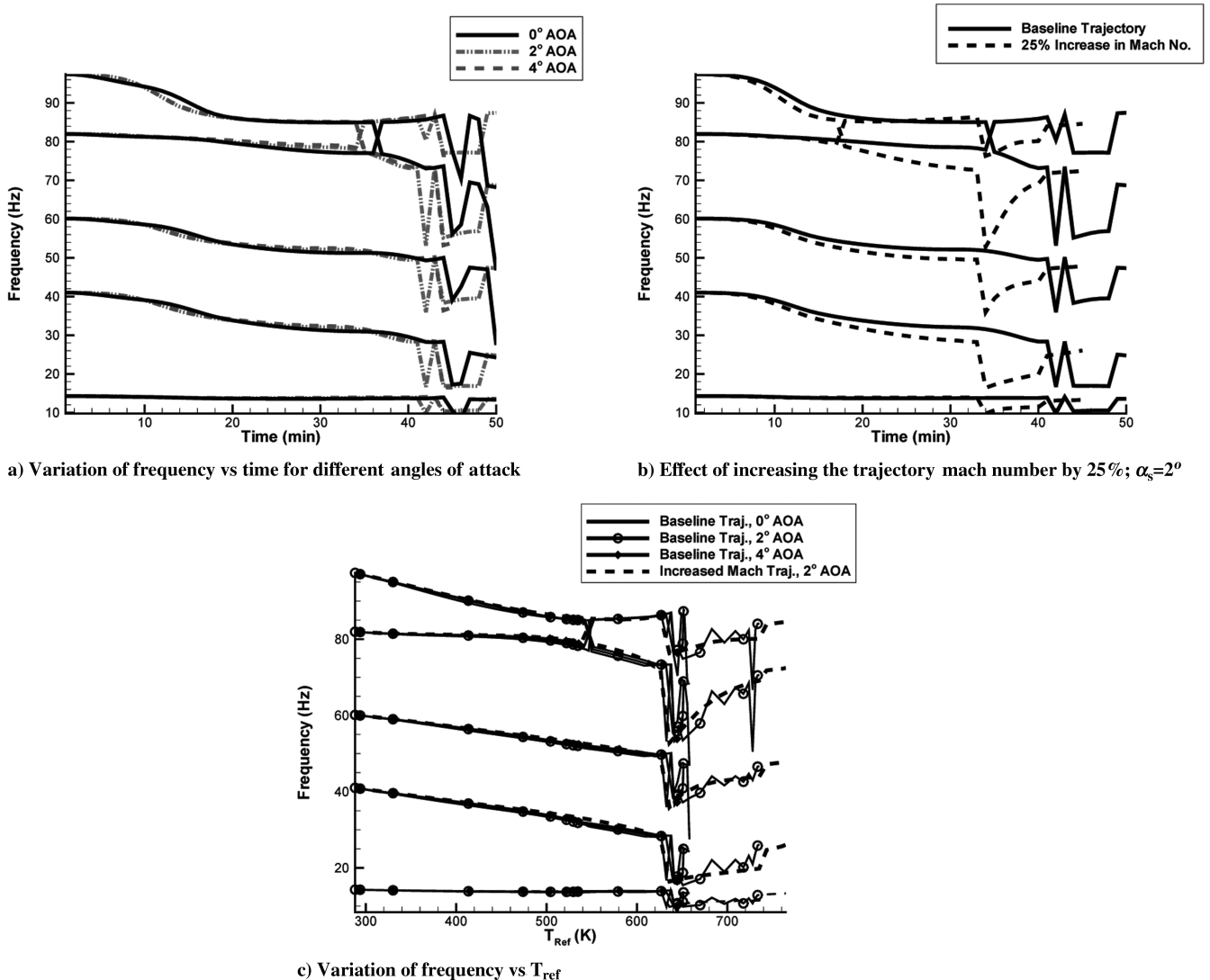

a) Variation of frequency vs time for different angles of attack

b) Effect of increasing the trajectory mach number by 25%; $\alpha_s = 2^\circ$

c) Variation of frequency vs T_{ref}

Fig. 22   Natural frequencies of the modified low-aspect-ratio wing operating along a representative hypersonic trajectory.

Table 10 Maximum percent change in the prebuckled modal frequencies of the heated low-aspect-ratio wing operating on a representative trajectory (a negative sign indicates a decrease in frequency)

Case	Mode 1	Mode 2	Mode 3	Mode 4	Mode 5
$\alpha_s = 0$ deg	−2.4%	−31.0%	−16.9%	5.8%	−24.4%
$\alpha_s = 2$ deg	−2.8%	−30.8%	−17.3%	5.3%	−24.7%
$\alpha_s = 4$ deg	−1.2%	−30.6%	−16.6%	6.2%	−24.7%
Increased Mach no.	−2.1%	−31.2%	−17.6%	5.6%	−25.3%

equations, is sensitive to two CFL3D pseudotime subiteration scheme parameters: namely, the number of subiterations used and CFL_τ. A case-by-case study must be conducted to ensure that these parameters have appropriate values.

4) The aeroelastic behavior of the low-aspect-ratio wing obtained using piston theory and Euler aerodynamics is similar for the configuration considered. The flutter Mach number and dynamic pressure at flutter are within 5 and 8%, respectively, for all altitudes considered.

5) The effect of viscosity is not significant for the aeroelastic behavior of the low-aspect-ratio wing at moderate-to-high altitudes and Mach numbers. The Mach number and dynamic pressure at flutter are within 8 and 10%, respectively, between the viscous and inviscid results for $13.0 < M < 35.0$ and altitudes of 40,000 to 70,000 ft. Conversely at 30,000 ft and lower, the effect of viscosity is substantial, resulting in up to 20 and 60% error in flutter Mach number and dynamic pressure at flutter, respectively. However, hypersonic vehicles cannot operate at hypersonic speeds at such an altitude.

6) The relatively low values of the reduced frequencies observed for the low-aspect-ratio wing can be used to justify the quasi-steady nature of the piston theory loads. This implies that the computational cost associated with solving the unsteady Euler and Navier–Stokes equations can be reduced by introducing a quasi-steady flow assumption in an appropriate manner.

7) The aeroelastic behavior of the configurations considered is relatively insensitive to grid resolution as long as a sufficient number of grid points are within the shock layer of the flow.

8) The presence of aerodynamic heating on a low-aspect-ratio cantilever structure, such as a fin and/or control surface on a hypersonic vehicle, results in thermal stresses due to warping restraint at the root. This, combined with material-property degradation, generally reduces the natural frequencies of the structure by 20–30%. Increasing the Mach number decreases the time elapsed before thermal buckling occurs. Changes in frequency are similar for various Mach numbers when plotted as a function of leading-edge temperature.

9) Angle of attack may be important for the aerothermoelastic analysis of a structure because it introduces additional thermal stresses that can significantly degrade the stiffness of the structure for a given reference temperature or point in time. In an extreme case of sustained cruise, the free-vibration frequencies of the wing were reduced by 50%. However, for the heating conditions encountered along a representative trajectory, the frequencies were less sensitive to angle of attack.

10) The flutter margin of the wing along a representative hypersonic trajectory is reduced by up to 40% due to aerodynamic heating. Furthermore, the flutter margin is sensitive to Mach number. Increasing the Mach number by 25% reduces the flutter margin by an additional 30%. Angle of attack did not affect the flutter margin along a representative trajectory.

11) For the cases considered here, the virtual dynamic pressure values required to induce flutter along the trajectory are at least an order of magnitude higher than freestream values, which demonstrates the benefits of vehicle operation at high altitudes.

12) Thermal buckling of the wing structure is identified as the critical mode of failure for the system, emphasizing the need for advanced materials and/or active cooling systems on hypersonic vehicles. For the trajectory considered, the wing buckles in less than half the time required to complete the mission objective.
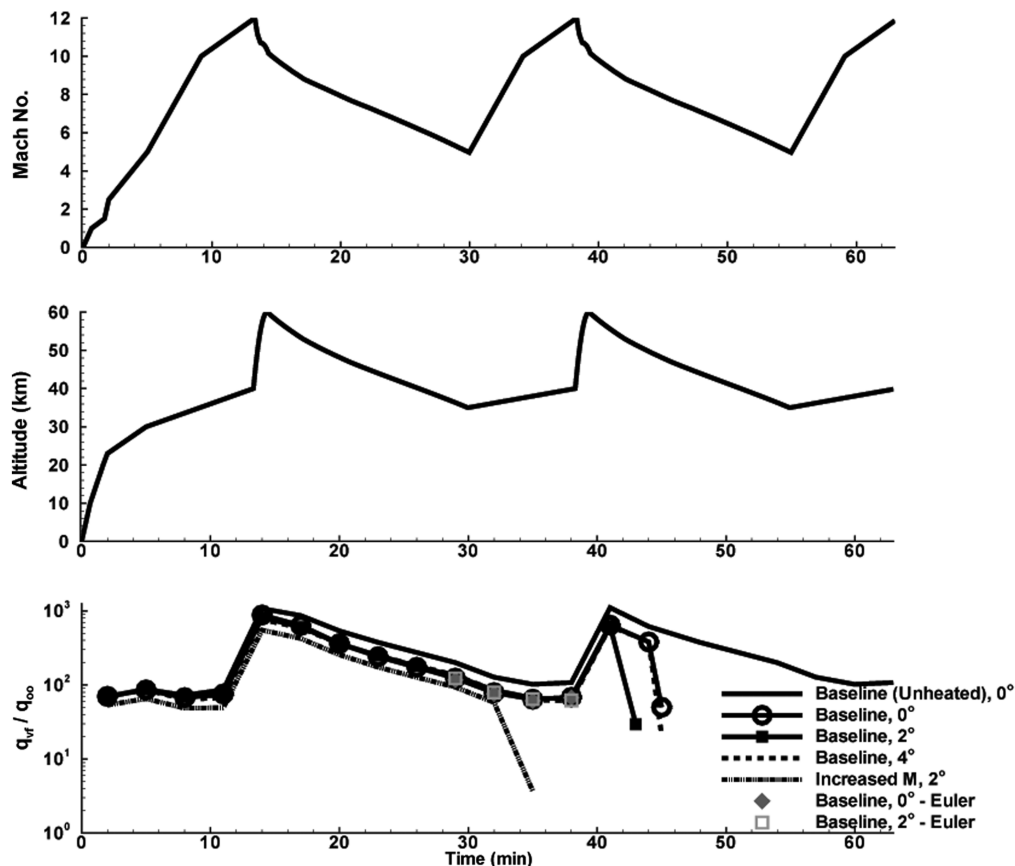

Fig. 23 Aerothermoelastic flutter margin of the modified low-aspect-ratio wing along a representative hypersonic trajectory.

13) The results presented can be considered to provide a partial verification of the aeroelastic capabilities of the CFL3D code for the hypersonic flow regime.

Acknowledgments

References

[1] Anderson, J. D., *Hypersonic and High Temperature Gas Dynamics*, McGraw–Hill, New York, 1989.

[2] Nydick, I., *Studies in Hypersonic Aeroelasticity*, Ph.D. Thesis, Univ. of California, Los Angeles, 2000.

[3] McClinton, C., "X-43 Scramjet Power Breaks the Hypersonic Barrier: Dryden Lectureship in Research for 2006," 44th AIAA Aerospace Sciences Meeting and Exhibit, Reno NV, AIAA Paper 2006-1, 2006.

[4] Neuenhahn, T., Olivier, H., and Paull, A., "Development of the Hyshot Stability Demonstrator," 25th AIAA Aerodynamic Measurement Technology and Ground Testing Conference, San Francisco, AIAA Paper 2006-2960, 2006.

[5] Walker, W., and Rodgers, F., "Falcon Hypersonic Technology Overview," 13th International Space Planes and Hypersonic Systems and Technologies Conference, Capua, Italy, AIAA Paper 2005-3253, 2005.

[6] Ricketts, R., Noll, T., Whitlow, W., and Huttsell, L., "An Overview of Aeroelasticity Studies for the National Aerospace Plane," *34th AIAA/ ASME/ASCE/AHS/ASC Structures, Structural Dynamics and Materials Conference*, AIAA, Washington, D.C., 1993, pp. 152–162; also AIAA Paper 93-1313, 1993.

[7] Gupta, K. K., Voelker, L. S., Bach, C., Doyle, T., and Hahn, E., "CFD-Based Aeroelastic Analysis of the X-43 Hypersonic Flight Vehicle," 39th Aerospace Sciences Meeting and Exhibit, Reno, NV, AIAA Paper 2001-0712, 2001.

[8] Berry, S. A., Horvath, T. J., Hollis, B. R., Thompson, R. A., and Hamilton, H. H., "X-33 Hypersonic Boundary Layer Transition," 33rd AIAA Thermophysics Conference, Norfolk, VA, AIAA Paper 99-3560, 1999.

[9] Riley, C. J., Kleb, W. L., and Alter, S. J., "Aeroheating Predictions for X-34 Using an Inviscid-Boundary Layer Method," 36th AIAA Aerospace Sciences Meeting and Exhibit, Reno, NV, AIAA Paper 98-0880, Jan. 1998.

[10] Bertin, J. J., *Hypersonic Aerothermodynamics*, AIAA, Washington, D.C., 1994.

[11] Dugundji, J., and Calligeros, J., "Similarity Laws for Aerothermoelastic Testing," *Journal of the Aerospace Sciences*, Vol. 29, No. 8, Aug. 1962, pp. 935–950.

[12] Bisplinghoff, R. L., and Dugundji, J., *Influence of Aerodynamic Heating on Aeroelastic Phenomena*, Pergamon, New York, 1958, pp. 288–312.

[13] Rogers, M., "Aerothermoelasticity," *Aerospace Engineering*, Oct. 1958, pp. 34–43.

[14] Garrick, I. E., "A Survey of Aerothermoelasticity," *Aerospace Engineering*, Jan. 1963, pp. 140–147.

[15] Hedgepeth, J., and Widmayer, E., "Dynamic and Aeroelastic Problems of Lifting Re-Entry Bodies," *Aerospace Engineering*, Jan. 1963, pp. 148–153.

[16] Laidlaw, W. R., and Wyker, J. H., "Potential Aerothermoelastic Problems Associated with Advanced Vehicle Design," *Aerospace Engineering*, Jan. 1963, pp. 154–164.

[17] Xue, D. Y., and Mei, C., "Finite Element Two-Dimensional Panel Flutter at High Supersonic Speeds and Elevated Temperature," *31st AIAA/ASME/ASCE/AHS/ASC Structures, Structural Dynamics and Materials Conference*, AIAA, Washington, D.C., 1990, pp. 1464–1475; also AIAA Paper 90-0982, 1990.

[18] Gray, E. G., and Mei, C., "Large-Amplitude Finite Element Flutter Analysis of Composite Panels in Hypersonic Flow," *33rd AIAA/ASME/ ASCE/AHS/ASC Structures, Structural Dynamics and Materials Conference*, AIAA, Washington, D.C., 1992, pp. 492–512; also AIAA Paper 92-2130, 1992.

[19] Abbas, J. F., and Ibrahim, R. A., "Nonlinear Flutter of Orthotropic Composite Panel Under Aerodynamic Heating," *AIAA Journal*, Vol. 31, No. 8, 1993, pp. 1478–1488. doi:10.2514/3.11798

[20] Bein, T., Friedmann, P., Zhong, X., and Nydick, I., "Hypersonic Flutter of a Curved Shallow Panel with Aerodynamic Heating," 34th AIAA/ ASME/ASCE/AHS/ASC Structures, Structural Dynamics and Materials Conference, La Jolla, CA, AIAA Paper 93-1318, 1993.

[21] Nydick, I., Friedmann, P. P., and Zhong, X., "Hypersonic Panel Flutter Studies on Curved Panels," *36th AIAA/ASME/ASCE/AHS/ASC Structures, Structural Dynamics and Materials Conference*, AIAA, Washington, D.C., 1995, pp. 2995–3011; also AIAA Paper 95-1485, Apr. 1995.

[22] Mei, C., Abdel-Motagly, K., and Chen, R., "Review of Nonlinear Panel Flutter at Supersonic and Hypersonic Speeds," *Applied Mechanics Reviews*, Vol. 52, 1999, pp. 321–332.

[23] Spain, C., Zeiler, T. A., Bullock, E., and Hodge, J. S., "A Flutter Investigation of All-Moveable NASP-Like Wings at Hypersonic Speeds," 34th AIAA/ASME/ASCE/AHS/ASC Structures, Structural Dynamics and Materials Conference, La Jolla, CA, AIAA Paper 93-1315, 1993.

[24] Scott, R. C., and Pototzky, A. S., "A Method of Predicting Quasi-Steady Aerodynamics for Flutter Analysis of High Speed Vehicles Using Steady CFD Calculations," *34th AIAA/ASME/ASCE/AHS/ASC Structures, Structural Dynamics and Materials Conference*, AIAA, Washington, D.C., 1993, pp. 595–603; also AIAA Paper 93-1364, 1993.

[25] Spain, C., Zeiler, T. A., Gibbons, M. D., Soistmann, D. L., Pozefsky, P., DeJesus, R. O., and Brannon, C. P., "Aeroelastic Character of a National Aerospace Plane Demonstrator Concept," *34th AIAA/ASME/ ASCE/AHS/ASC Structures, Structural Dynamics and Materials Conference*, AIAA, Washington, D.C., Apr. 1993, pp. 163–170.

[26] Rodgers, J. P., "Aerothermoelastic Analysis of a NASP-Like Vertical Fin," 33rd AIAA/ASME/ASCE/AHS Structures, Structural Dynamics and Materials Conference, Dallas, TX, AIAA Paper 92-2400, Apr. 1992.

[27] Heeg, J., Zeiler, T., Pototzky, A., Spain, C., and Engelund, W., "Aerothermoelastic Analysis of a NASP Demonstrator Model," *34th AIAA/ASME/ASCE/AHS/ASC Structures, Structural Dynamics and Materials Conference*, AIAA, Washington, D.C., 1993, pp. 617–627; also AIAA Paper 93-1366, 1993.

[28] Heeg, J., and Gilbert, M. G., "Active Control of Aerothermoelastic Effects for a Conceptual Hypersonic Aircraft," *Journal of Aircraft*, Vol. 30, No. 4, 1993, pp. 453–458. doi:10.2514/3.56890

[29] Blades, E., Ruth, M., and Fuhrman, D., "Aeroelastic Analysis of the X-34 Launch Vehicle," *40th AIAA/ASME/ASCE/AHS/ ASC Structures, Structural Dynamics and Materials Conference*, AIAA, Reston, VA, 1999, pp. 1321–1331; also AIAA Paper 99-1352, 1999.

[30] Nydick, I., and Friedmann, P. P., "Aeroelastic Analysis of a Generic Hypersonic Vehicle," *CEAS/AIAA/ICASE/NASA Langley International Forum on Aeroelasticity and Structural Dynamics*, NASA CP-1999-209136/PT2, NASA Langley Research Center, Hampton, VA, June 1999, pp. 777–810.

[31] Friedmann, P. P., McNamara, J. J., Thuruthimattam, B. J., and Nydick, I., "Aeroelastic Analysis of Hypersonic Vehicles," *Journal of Fluids and Structures*, Vol. 19, No. 5, 2004, pp. 681–712. doi:10.1016/j.jfluidstructs.2004.04.003

[32] Krist, S. L., Biedron, R. T., and Rumsey, C. L., "CFL3D User's Manual (Ver. 5.0)," NASA TM 1998-208444, 1997.

[33] Bartels, R. E., "Mesh Strategies for Accurate Computation of Unsteady Spoiler and Aeroelastic Problems," *Journal of Aircraft*, Vol. 37, No. 3, May 2000, pp. 521–525.

[34] Robinson, B. A., Batina, J. T., and Yang, H. T., "Aeroelastic Analysis of Wings Using the Euler Equations with a Deforming Mesh," *Journal of Aircraft*, Vol. 28, No. 11, Nov. 1991, pp. 781–788. doi:10.2514/3.46096

[35] Cunningham, H. J., Batina, J. T., and Bennett, R. M., "Modern Wing Flutter Analysis by Computational Fluid Dynamic Methods," *Journal of Aircraft*, Vol. 25, No. 10, 1988, pp. 962–968. doi:10.2514/3.45686

[36] Lee-Rausch, E. M., and Batina, J. T., "Wing Flutter Boundary Prediction Using Unsteady Euler Aerodynamic Method," *34th AIAA/ ASME/ASCE/AHS Structures, Structural Dynamics and Materials Conference*, AIAA, Washington, D.C., 1993, pp. 1019–1029; also AIAA Paper 93-1422, 1993.

[37] Lee-Rausch, E. M., and Batina, J. T., "Calculation of AGARD Wing 445.6 Flutter Using Navier–Stokes Aerodynamics," AIAA 11th Applied Aerodynamics Conference, Hampton, VA, AIAA Paper 93-3476, 1993.

[38] Silva, W., and Bartels, R., "Development of Reduced-Order Models for Aeroelastic Analysis and Flutter Prediction Using the CFL3Dv6.0 code," *Journal of Fluids and Structures*, Vol. 19, No. 6, 2004, pp. 729–745.
doi:10.1016/j.jfluidstructs.2004.03.004

[39] Batina, J. T., "Unsteady Euler Airfoil Solutions Using Unstructured Dynamic Meshes," *AIAA Journal*, Vol. 28, No. 8, 1990, pp. 1381–1388.
doi:10.2514/3.25229

[40] Tezduyar, T. E., Behr, M., and Liou, J., "A New Strategy for Finite Element Computations Involving Moving Boundaries and Interfaces—The Deforming-Spatial-Domain/Space–Time Procedure, 1: The Concept and the Preliminary Numerical Tests," *Computer Methods in Applied Mechanics and Engineering*, Vol. 94, No. 3, Feb. 1992, pp. 339–351.
doi:10.1016/0045-7825(92)90059-S

[41] Hughes, T. J. R., and Hulbert, G. M., "space–time Finite Element Methods for Elastodynamics: Formulations and Error Estimates," *Computer Methods in Applied Mechanics and Engineering*, Vol. 66, No. 3, Feb. 1988, pp. 339–363.
doi:10.1016/0045-7825(88)90006-0

[42] Patil, M. J., Hodges, D. H., and Cesnik, C. E. S., "Nonlinear Aeroelastic Analysis of Complete Aircraft in Subsonic Flow," *Journal of Aircraft*, Vol. 37, No. 5, Sept. 2000, pp. 753–760.

[43] Donea, J., Guiliani, S., and Halleux, J. P., "An Arbitrary Lagrangian-Eulerian Finite Element Method for Transient Dynamic Fluid–Structure Interactions," *Computer Methods in Applied Mechanics and Engineering*, Vol. 33, Nos. 1–3, Sept. 1982, pp. 689–723.
doi:10.1016/0045-7825(82)90128-1

[44] Bendiksen, O. O., "A New Approach to Computational Aeroelasticity," *AIAA/ASME/ASCE/AHS/ASC 32nd Structure, Structural Dynamics and Materials Conference*, AIAA, Washington, D.C., 1991, pp. 1712–1727; also AIAA Paper 91-0939, 1991.

[45] Farhat, C., Lesoinne, M., and Maman, N., "Mixed Explicit/Implicit Time Integration of Coupled Aeroelastic Problems: Three-Field Formulation, Geometric Conservation and Distributed Solution," *International Journal for Numerical Methods in Fluids*, Vol. 21, No. 10, 1995, pp. 807–835.
doi:10.1002/fld.1650211004

[46] Tran, H., and Farhat, C., "An Integrated Platform for the Simulation of Fluid-Structure-Thermal Interaction Problems," *43rd AIAA/ASME/ASCE/AHS Structures, Structural Dynamics and Materials Conference*, Denver, CO, AIAA Paper 2002-1307, Apr. 2002.

[47] Stephens, C. H., Arena, A. S., Jr., and Gupta, K. K., "Application of the Transpiration Method for Aeroservoelastic Prediction Using CFD," *39th AIAA/ASME/ASCE/AHS/ASC Structures, Structural Dynamics, and Materials Conference and Exhibit*, Long Beach, CA, AIAA Paper 98-2071, 1998.

[48] Hartwich, P., and Agrawal, S., "Perturbing Multiblock Patched Grids in Aeroelastic Design Optimization Applications," AIAA Paper 97-2038, June 1997.

[49] Bartels, R. E., Rumsey, C. L., and Biedron, R. T., "CFL3D Ver. 6.4–General Usage and Aeroelastic Analysis," NASA TM -2006-214301, 2006.

[50] Bartels, R. E., "Finite Macro-Element Mesh Deformation in a Structured Multi-Block Navier–Stokes Code," NASA TM -2005-213789, 2005.

[51] Thompson, J., Bharat, S., and Weatherrill, N., *Handbook of Grid Generation*, CRC Press, Boca Raton, FL, 1998.

[52] Matsuzaki, Y., and Ando, Y., "Estimation of Flutter Boundary from Random Responses Due to Turbulence at Subcritical Speeds," *Journal of Aircraft*, Vol. 18, No. 10, 1981, pp. 862–868.
doi:10.2514/3.44737

[53] Torii, H., and Matsuzaki, Y., "Flutter Margin Evaluation for Discrete-Time Systems," *Journal of Aircraft*, Vol. 38, No. 1, 2001, pp. 42–47.

[54] Bae, J., Kim, J., Lee, I., Matsuzaki, Y., and Inman, D., "Extension of Flutter Prediction Parameter for Multimode Flutter Systems," *Journal of Aircraft*, Vol. 42, No. 1, 2005, pp. 285–288.
doi:10.2514/1.6440

[55] Pak, C. G., and Friedmann, P. P., "New Time Domain Technique for Flutter Boundary Identification," *AIAA Dynamics Specialist Conference*, AIAA, Washington, D.C., 1992, pp. 201–214; also AIAA Paper 92-2102, Apr. 1992.

[56] McNamara, J. J., and Friedmann, P. P., "Flutter-Boundary Identification for Time-Domain Computational Aeroelasticity," *AIAA Journal*, Vol. 45, No. 7, July 2007, pp. 1546–1555.
doi:10.2514/1.26706

[57] Ashley, H., and Zartarian, G., "Piston Theory–A New Aerodynamic Tool for the Aeroelastician," *Journal of the Aeronautical Sciences*, Vol. 23, No. 12, 1956, pp. 1109–1118.

[58] Lighthill, M. J., "Oscillating Airfoils at High Mach Numbers," *Journal of the Aeronautical Sciences*, Vol. 20, No. 6, June 1953, pp. 402–406.

[59] Anderson, J. D., *Aerothermodynamics: A Tutorial Discussion*, AIAA, Washington, D.C., 1992, pp. 3–57.

[60] Bisplinghoff, R. L., "Some Structural and Aeroelastic Considerations of High-Speed Flight," *Journal of the Aerospace Sciences*, Vol. 23, No. 4, Apr. 1956, pp. 289–329.

[61] Garrick, I. E., "Aeroelasticity–Frontiers and Beyond," *Journal of Aircraft*, Vol. 13, Sept. 1976, pp. 641–657.
doi:10.2514/3.58696

[62] Thornton, E., "Thermal Structures: Four Decades of Progress," *Journal of Aircraft*, Vol. 29, No. 3, May–June 1992, pp. 485–497.
doi:10.2514/3.46187

[63] Thornton, E., *Thermal Structures for Aerospace Applications*, AIAA, Reston, VA, 1996.

[64] Budiansky, B., and Mayers, J., "Influence of Aerodynamic Heating on the Effective Torsional Stiffness of Thin Wings," *Journal of the Aeronautical Sciences*, Vol. 23, No. 12, Dec. 1956, pp. 1081–1093.

[65] Almroth, J. A., Bailie, J. A., and Stanley, G. M., "Vibration Analysis of Heated Plates," *AIAA Journal*, Vol. 15, No. 12, 1977, pp. 1691–1695.
doi:10.2514/3.7474

[66] Bailey, C. D., "Vibration of Thermally Stressed Plates with Various Boundary Conditions," *AIAA Journal*, Vol. 11, No. 1, 1973, pp. 14–19.
doi:10.2514/3.6666

[67] McNamara, J., "Aeroelastic and Aerothermoelastic Behavior of Two and Three Dimensional Surfaces in Hypersonic Flow," Ph.D. Thesis, Univ. of Michigan, Ann Arbor, MI, 2005.

[68] Rasmussen, M., *Hypersonic Flow*, Wiley, New York, 1994.

[69] Thuruthimattam, B. J., "Fundamental Studies in Hypersonic Aeroelasticity Using Computational Methods," Ph.D. Thesis, Univ. of Michigan, Ann Arbor, MI, 2005.

[70] Biot, M. A., "Influence of Thermal Stresses on the Aeroelastic Stability of Supersonic Wings," *Journal of the Aeronautical Sciences*, Vol. 24, No. 6, June 1957, pp. 418–420.

[71] Bisplinghoff, R. L., Ashley, H., and Halfman, R. L., *Aeroelasticity*, Addison Wesley, Reading, MA, 1955.

[72] Reissner, E., and Stein, M., "Torsion and Transverse Bending of Cantilever Plates," NACA TN 2369, 1951.

[73] Crawley, E. F., and Dugundji, J., "Frequency Determination and Non-Dimensionalization for Composite Cantilever Plates," *Journal of Sound and Vibration*, Vol. 72, No. 1, 1980, pp. 1–10.
doi:10.1016/0022-460X(80)90703-8

[74] Gern, F., and Librescu, L., "Aeroelastic Tailoring of Composite Wings Exhibiting Nonclassical Effects and Carrying External Stores," *Journal of Aircraft*, Vol. 37, No. 6, 2000, pp. 1097–1104.

[75] "MSC.Nastran Reference Manual," MSC Software Corp., Santa Ana, CA, 2001.

[76] Bailey, C. D., "Vibration and Local Edge Buckling of Thermally Stressed, Wedge Airfoil Cantilever Wings," AIAA Dynamics Specialists Conference, Williamsburg, VA, AIAA Paper 73-327, 1973.

[77] Vosteen, L. F., "Effect of Temperature on Dynamic Modulus of Elasticity of Some Structural Alloys," NACA TN 4348, 1958.

[78] *Thermophysical Properties of Matter*, Vol. 13, IFI/Plenum, , New York, 1970.

[79] Ellis, D. A., Pagel, L. L., and Schaeffer, D. M., "Design and Fabrication of a Radiative Actively Cooled Honeycomb Sandwich Structural Panel for a Hypersonic Aircraft," NASA CR 2957, 1978.

[80] Thuruthimattam, B. J., Friedmann, P. P., McNamara, J. J., and Powell, K. G., "Modeling Approaches to Hypersonic Aerothermoelasticity with Application to Reusable Launch Vehicles," 44th AIAA/ASME/ASCE/AHS Structures, Structural Dynamics and Materials Conference, Norfolk, VA, AIAA Paper 2003-1967, 2003.

[81] McNamara, J. J., Friedmann, P. P., Powell, K. G., Thuruthimattam, B. J., and Bartels, R. E., "Three-dimensional Aeroelastic and Aerothermoelastic Behavior in Hypersonic Flow," 46th AIAA/ASME/ASCE/AHS Structures, Structural Dynamics and Materials Conference, Austin, TX, AIAA Paper 2005-2175, 2005.

[82] Cazier, F. W., Doggett, R. V., and Ricketts, R. H., "Structural Dynamic and Aeroelastic Considerations for Hypersonic Vehicles," 32nd AIAA/ASME/ASCE/AHS/ASC Structures, Structural Dynamics and Materials Conference, Baltimore, MD, AIAA Paper 1991-1255Apr. 1991.

[83] Lu, P., "Trajectory Optimization for the National Aerospace Plane," NASA CR-194618, Nov. 1993.

[84] Hankey, W. L., *Re-Entry Aerodynamics*, AIAA, Reston, VA, 1998.